Double-differential fragmentation cross-section measurements of 95 MeV/nucleon ^{12}C beams on thin targets for hadron therapy

J. Dudouet,[1,*] D. Juliani,[2] M. Labalme,[1] D. Cussol,[1] J. C. Angélique,[1] B. Braunn,[3] J. Colin,[1] Ch. Finck,[2] J. M. Fontbonne,[1] H. Guérin,[1] P. Henriquet,[4] J. Krimmer,[4] M. Rousseau,[2] M. G. Saint-Laurent,[5] and S. Salvador[1]

[1]*LPC Caen, ENSICAEN, Université de Caen, CNRS/IN2P3, Caen, France*

[2]*Institut Pluridisciplinaire Hubert Curien Strasbourg, France*

[3]*CEA/Saclay, DSM/Irfu/SPhN, Gif-sur-Yvette, France*

[4]*IPN Lyon, Université de Lyon, Université Lyon 1, CNRS/IN2P3, Villeurbanne, France*

[5]*GANIL, Caen, France*

(Received 27 March 2013; published 12 August 2013)

During therapeutic treatment with heavy ions like carbon, the beam undergoes nuclear fragmentation and secondary light charged particles, in particular protons and α particles, are produced. To estimate the dose deposited into the tumors and the surrounding healthy tissues, an accurate prediction on the fluences of these secondary fragments is necessary. Nowadays, a very limited set of double differential carbon fragmentation cross sections are being measured in the energy range used in hadron therapy (40 to 400 MeV/nucleon). Therefore, new measurements are performed to determine the double differential cross section of carbon on different thin targets. This work describes the experimental results of an experiment performed on May 2011 at GANIL. The double differential cross sections and the angular distributions of secondary fragments produced in the ^{12}C fragmentation at 95 MeV/nucleon on thin targets (C, CH_2, Al, Al_2O_3, Ti, and PMMA) have been measured. The experimental setup will be precisely described, the systematic error study will be explained and all the experimental data will be presented.

DOI: 10.1103/PhysRevC.88.024606 PACS number(s): 25.70.Mn, 87.56.−v

I. INTRODUCTION

The use of carbon ion beams in hadron therapy to treat cancerous tumors is motivated by the highly localized dose distribution. The high carbon mass (compared to proton) leads to a smaller angular scattering and a higher dose deposition at the end of the radiation range (i.e., at the Bragg peak). Moreover, the biological efficiency, which is strongly correlated to the linear energy transfer (LET), is higher for carbon ions in the Bragg peak region. Carbon ions allow thus to better target the tumor while preserving the surrounding healthy tissues. However, to keep the benefits of carbon ions in radiotherapy, a very high accuracy on the dose deposition is required ($\pm$3% and $\pm$1 mm). The physical dose deposition is affected by the fragmentation of the ions along their penetration path in the human tissues [1]. As a consequence, the number of incident ions reaching the tumor is reduced for example up to 70% for 400 MeV/nucleon ^{12}C in water. The carbon beam fragmentation in the human body leads to a mixed radiation field composed of lighter fragments of higher ranges and angular distributions with respect to the primary ions. These lighter fragments have different relative biological effectiveness (RBE) which contribute to the deposited dose all along the carbon path. These effects, due to the carbon fragmentation, result in a new spatial dose distribution, particularly on healthy tissues. This must be taken into account for the evaluation of the biological dose [2] by accurately evaluating the fragmentation processes.

Simulation codes are used to compute the transportation of ions in the matter but the constraints on nuclear models and fragmentation cross sections in the energy range used in hadron therapy (up to 400 MeV/nucleon) are not yet sufficient to reproduce the fragmentation processes with the required accuracy for clinical treatments [3–5]. Nuclear cross sections are critical inputs for these simulation frameworks. In particular there is a lack of experimental cross section data available for light ions on light targets in the energy range from 30 to 400 MeV/nucleon. These experimental data are necessary to benchmark the Monte Carlo codes for their use in hadron therapy.

To improve the knowledge on the ^{12}C fragmentation processes, experiments have been performed in Japan and in Europe for more than 15 years. Measurements of light charged fragment production in water and PMMA have been performed by the Japanese treatment centers (Chiba and Hyogo) [6–8] and by the GSI biophysics department [9–11] in the energy range from 200 to 400 MeV/nucleon. All these measurements were used to determine the integrated flux and energy distributions of the fragments relative to the penetration depth in water equivalent matter. To extend these data to the lowest energies, a first integral experiment on thick PMMA targets has been performed by our collaboration in May 2008 at GANIL (France) [12]. Energy and angular distributions of the fragments produced by nuclear reactions of a 95 MeV/nucleon ^{12}C beam on thick PMMA targets have been obtained. Comparisons between Monte Carlo simulation codes (FLUKA [13], INCL [14], and GEANT4 [15]) have been performed [3,4,16] using different physics processes (binary cascade or quantum molecular dynamic). These simulations have shown discrepancies up to one order of magnitude for

*Corresponding author: dudouet@lpccaen.in2p3.fr

the production rates of fragments. The angular and energy distributions were also not well reproduced.

Nevertheless, it is difficult to constrain the nuclear reaction models by a direct comparison to thick target experiments. To improve the models and reach the accuracy required for a reference simulation code for hadron therapy, experiments on thin targets were planned. An experiment has been performed at 62 MeV/nucleon on carbon target in Catania [5]. An other one has been performed at 400 MeV/nucleon on carbon target at GSI by the FIRST collaboration [17]. A third experiment has been performed by our collaboration on May 2011 at GANIL to study carbon reaction on C, H, O, Al, and ^{nat}Ti targets at 95 MeV/nucleon. The data analysis method has already been described in a previous paper [18]. In the following part, the experimental setup will be recalled, in a second part, the study of the systematic errors will be detailed and finally, in the last part, the experimental results will be presented.

II. EXPERIMENTAL SETUP

The experiment used the ECLAN reaction chamber at the GANIL G22 beam line. In order to obtain the double differential fragmentation cross sections of carbon on carbon, oxygen, hydrogen, and calcium targets (which represent around 95% of the human body composition), a ^{12}C beam at 94.6 ± 0.09 MeV/nucleon was sent on different thin targets [C, CH_2, Al, Al_2O_3, ^{nat}Ti, PMMA ($C_5H_8O_2$)]. We made here the approximation that the cross sections for the calcium target must be close to those of titanium ($^{40}_{20}$Ca $\sim$ $^{48}_{22}$Ti). The target area densities are about $\sim$50 mg/cm^2. The area densities [density (ρ)$\times$ thickness (th)] given values have been measured with a high precision balance leading to a relative error on the area densities of 1%. The target characteristics are described in Table I.

For the charged particles detection, the setup consists of four $\Delta E_{\text{thin}}/\Delta E_{\text{thick}}/E$ telescopes mounted two by two on two stages that allows rotation inside the chamber from 0° to 43° with 2° steps at a distance of 204 mm behind the target. The accuracy on the angles has been estimated to $\pm 1°$ due to mechanical uncertainties on the position of the rotating stages. A fifth telescope was mounted downstream, at a fixed angle of 4° and a distance of 820 mm behind the target (cf. Fig. 1). The geometrical properties of the experimental setup are described in Table II.

The five $\Delta E_{\text{thin}}/\Delta E_{\text{thick}}/E$ telescopes consist in two silicon detectors followed by a 10 cm thick CsI(Tl) scintillator. The thicknesses of the silicon detectors were $\sim$150 μm and $\sim$1000 μm, respectively. To prevent interaction of the scintillation light emitted by the CsI with the thick silicon detector, a thin mylar sheet of 12 μm is placed between these two detectors. The silicon detectors and the CsI crystal have a diameter of 1.9 cm and 3 cm, respectively. The higher diameter of the scintillating crystal is used to prevent particles with high incidence angles to escape out of the crystal by scattering. The detector dimensions are summarized in Tables II and III. Acceptances given in the Table II are those of the thick silicon detectors. Indeed, the acquisition was triggered only if the thick silicon detector was hit. As the silicon detector thicknesses were not the same, an energy threshold has been used. This threshold has been calculated for each detected isotope and for the thickest of the thin silicon detectors (telescope n°1). The resulting energy thresholds are given in Table IV.

TABLE I. Target characteristics.

Targets	th (in μm)	$\rho \times$ th (in g cm^{-2})
C	250	0.0411
CH_2	500	0.0481
Ti	125	0.0576
Al	200	0.0540
Al_2O_3	150	0.0550
PMMA ($C_5H_8O_2$)	500	0.0642

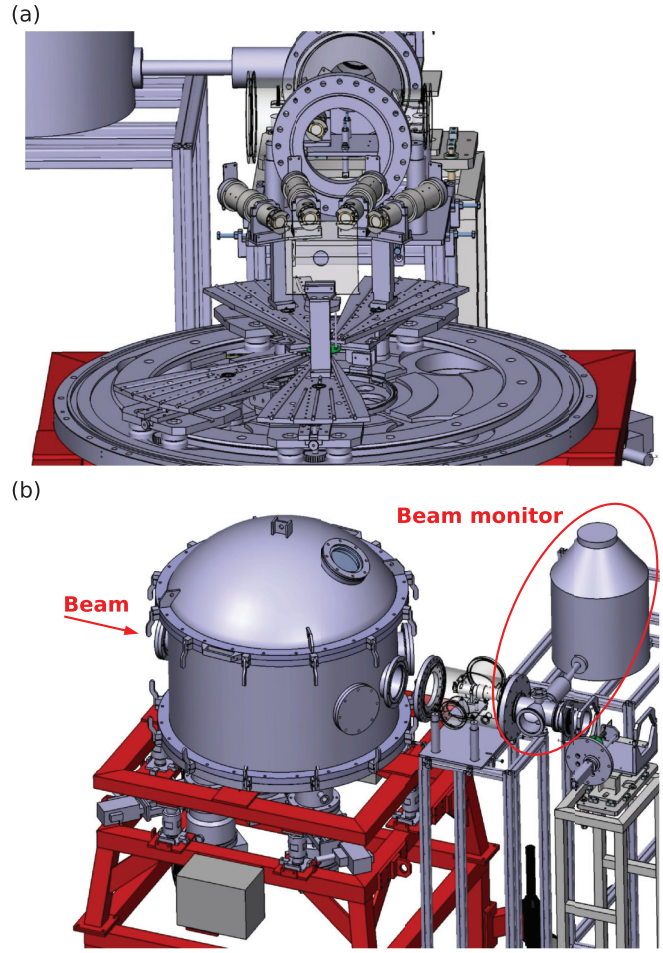

FIG. 1. (Color online) Representation of inside the vacuum chamber with the four rotating telescopes and the fixed telescope backward (a) and a larger view including the beam monitor (b).

TABLE II. Geometrical properties of the detectors.

	Telescope	Thin Si	Thick Si	CsI	Ω (msr)
Distance to the	1	820 (5)	828 (5)	834 (5)	0.43 (3)
target (mm)	2-3-4-5	204 (5)	212 (5)	218 (5)	6.6 (5)
Diameter	1$\rightarrow$5	1.954 cm	1.954 cm	3 cm	

TABLE III. Charged particles detectors thicknesses.

Telescope	Thin Si	Thick Si	CsI
1	161 μm	1011 μm	
2	159 μm	1014 μm	
3	160 μm	1014 μm	10 cm
4	152 μm	1011 μm	
5	101 μm	1018 μm	

To determine the number of incident ions, a beam monitor is placed after the reaction chamber. It is based on the measurement of fluorescence x rays emitted by a thin Ag foil (7 μm thick) which is set in the beam. X rays are detected by means of a Si(Li) detector located at 90° with respect to the beam direction. This detector is calibrated at different beam intensities ranging from 10^3 to 10^6 ions/s using a plastic scintillator intercepting the beam. The calibration is then extrapolated on the whole intensity range of the experiment (from 10^5 to 10^7 ions/s). The error on the beam intensity has been estimated of about 5% [18].

For the electronic part, a digital acquisition named FASTER developed in-house was used. A FASTER module contains one QDC (charge to digital converter) used for the CsI and an ADC (analog to digital converter) used for the silicon detectors.

III. SYSTEMATIC ERRORS STUDY

A detailed description of the analysis method is described in Dudouet *et al*. [18]. It has been performed using the KaliVeda framework developed by the INDRA collaboration [19,20]. However, systematic errors due to detector effects still have to be determined to finalize the analysis.

The ^{12}C fragmentation cross sections for a ${}^{A}_{Z}X$ fragment are obtained as follows:

$$\frac{d\sigma}{d\Omega}\left({}^{A}_{Z}X\right) = \frac{N_{{}^{A}_{Z}X} \times A_{\text{target}}}{N_{^{12}\text{C}} \times \Omega \times \rho \times \text{th} \times \mathcal{N}_{\text{A}}}, \qquad (1)$$

where $N_{{}^{A}_{Z}X}$ is the number of ${}^{A}_{Z}X$ fragments detected, A and Z are, respectively, the mass and charge of the fragment X, A_{target} is the target mass, $N_{^{12}\text{C}}$ is the number of incident carbon nuclei, Ω is the solid angle of the detector, $\rho \times$ th is the target area density and $\mathcal{N}_{\text{A}}$ is the Avogadro's number.

Errors on $N_{^{12}\text{C}}$, Ω and $\rho \times$ th have been discussed in the first part, therefore, it remains to determine the error on $N_{{}^{A}_{Z}X}$. This last term is coming from detector effects generating wrong identifications. As statistical errors are low, e.g., from 1% to 5% for the rare isotopes, the systematic errors are the largest sources of uncertainties and must be determined. A first source of systematic errors comes from the identification method. This error was already estimated to be of the order of 5% for most of the measurements [18]. In order to estimate other sources of systematic errors, Monte Carlo simulations have been conducted, taking into account the experimental setup.

The experimental setup has been simulated by using the version 9.4 of the GEANT4 Monte Carlo simulation [15]. Electromagnetic interactions were described by using the "electromagnetic standard package option 3". Regarding the inelastic processes, two GEANT4 models have been tested: the binary cascade for light ions [21] and then the G4QMD model [22]. The simulated data were then analyzed with exactly the same method as for the experimental data. Overall, two sources of errors were observed.

The first one is due to inelastic processes in the CsI detector. Some detected particles might encounter inelastic processes in the CsI. This leads to energy losses coming on one hand from the Q value of the reaction and neutrons which are not detected and on the other hand, from lighter fragments emitted with high incidences and leaving the detector. Moreover, even if all the fragments are stopped in the detector, their resulting emitted scintillation light is changed due to quenching effects in the scintillator [23] which depend on the charge and mass of the particles. Such cases will induce a part of wrong identification.

The second source of errors comes from the pile-up of two particles in a telescope. If two particles from the same ^{12}C event are detected in a single detector, it will appear as one particle which has deposited the energy of two detected particles. The identification of the two different particles is thus no longer feasible. It appears in the simulations that ∼4% of the events are due to a pile-up of two or more particles. According to simulation results, the main contribution is due to the detection of two α particles at the same time. Although this phenomenon only represents a few percent of the whole statistics, it must be taken into account. As shown in Fig. 4, the events coming from the pile-up of two α particles appears on the ^{6}He and on the ^{6}Li-^{7}Li identification lines in the ΔE-E matrix. As the CsI is larger than the thick silicon detector, it is possible for a particle to reach the CsI without crossing the thick silicon detector. The pile-up component on the ^{6}He corresponds to events with only one α detected in the thick silicon and the sum of two in the CsI. The component on the lithium isotopes corresponds to the detection of both α in all detectors. The measured cross sections of these three rare isotopes (^{6}He, ^{6}Li, and ^{7}Li) are then modified by the pile-up.

Although this phenomenon was observed in simulations with the two tested models, their respective quantities are strongly model dependent (cf. Fig. 2) and then, cannot be applied as an accurate correction on experimental data. Therefore, in order to remove the pile-up events from the ΔE-E matrix, an experimental method has been chosen by analyzing the CsI light output signal shape. Using the digital acquisition, different gates in time have been chosen on the QDC (fast, slow, total) to integrate the light emitted by the

TABLE IV. Energy threshold.

Isotope	^{1}H	^{2}H	^{3}H	^{3}He	^{4}He	^{6}He	^{6}Li	^{7}Li	^{7}Be	^{9}Be	^{10}Be	^{8}B	^{10}B	^{11}B	^{10}C	^{11}C	^{12}C
E_{th} (MeV)	4.0	5.2	6.1	14.2	16.0	18.6	29.9	31.7	44.3	48.6	50.5	60.6	65.8	68.1	81.3	84.2	86.9

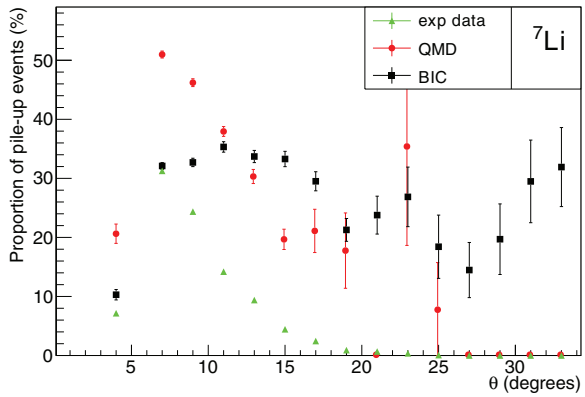

FIG. 2. (Color online) Proportion of pile-up events in the ^{7}Li statistic. The results have been estimated by GEANT4 simulations with BIC and QMD models. They are compared to the experimental results obtained with the CsI fast/slow matrix. Only statistical errors are shown.

scintillating crystal. By representing the fast component of the signal versus the slow one, a matrix on which each isotope is separated has been obtained (cf. Fig. 3). It turns out that the events that are coming from the pile-up of two α particles are clearly separated on this matrix. These pile-up events are located in a line which is between the ^{4}He and the ^{6}Li lines. It is thus possible to make a cut with the graphical tools of ROOT [24] on this pile-up contribution to remove it from the ΔE-E matrix. Figure 2 represents the proportion of pile-up events in the ^{7}Li statistics obtained by the experimental method and by GEANT4 simulations using BIC and QMD nuclear models. The QMD model seems to be more realistic but neither of the two models are able to correctly estimate the pile-up contribution.

Figure 4 represents an example of the pollution due to pile-up events on the ΔE-E matrix. In Fig. 4(a) are represented the pile-up events obtained by simulation with the QMD model of GEANT4 which seems to be the least far from the data. The light emitted by the CsI crystal has been simulated by using quenching formula described in Parlog *et al.* [25]. In Fig. 4(b) are represented the experimental ΔE-E matrix for the events selected as pile-up from the fast/slow matrix.

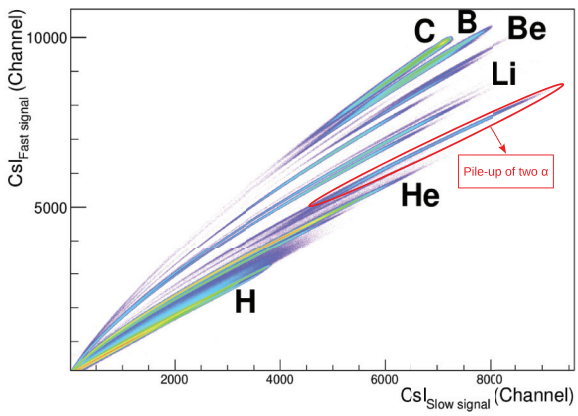

FIG. 3. (Color online) CsI(fast/slow) matrix. The different isotopes from protons to carbons are separated. The pile-up contribution is surrounded by red.

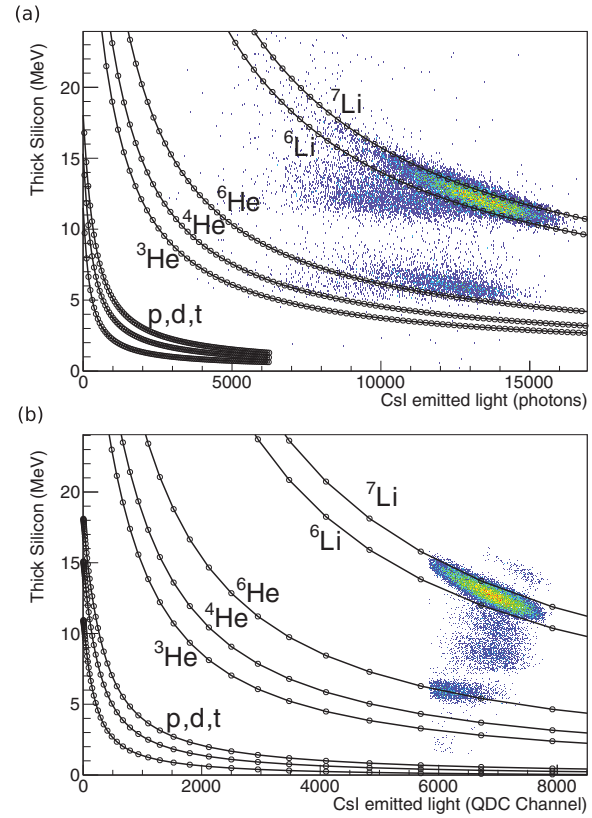

FIG. 4. (Color online) Background of the ΔE-E matrix due to pile-up of two α particles in a telescope from projected data made of the selection in Fig. 3. (a) Results obtained by GEANT4 simulations. (b) Experimental pollution due to events selected as pile-up from the fast/slow matrix.

Due to the proximity of the pile-up and ^{6}He events in the fast/slow matrix, some pile-up events could have been missed or some ^{6}He events could have been removed. The error bars for the ^{6}He distributions shown in the results were thus calculated as the difference between with and without pile-up correction, resulting conservative values. An example of the correction applied to the ^{7}Li distributions is given in Fig. 5 on which are represented the angular distribution (a) and the energy distribution at 7° (b) with and without corrections. The pile-up correction is mainly visible at low angles and high energies.

GEANT4 simulations have given a proportion of particles which fragment in the CsI of the order of several percents. In such cases, the inelastic processes lead to a loss of a part of the fragment's energy released in the CsI. It appears on the ΔE-E matrix as horizontal shift toward the lower energies. This phenomenon is affecting all the isotopes but is in general negligible. This is not the case for helium isotopes for which the α particles are produced ten times more than ^{3}He. Some α particles will then be identified as an ^{3}He. The proportion of α that have been identified as ^{3}He has been estimated to be about 5% which represents an error of 30% on the ^{3}He statistic. A correction has been done to the ^{3}He distributions by using the fast/slow components of the CsI light output.

Apart from these major error sources, the simulations were used to determine the percentage of well-identified particles

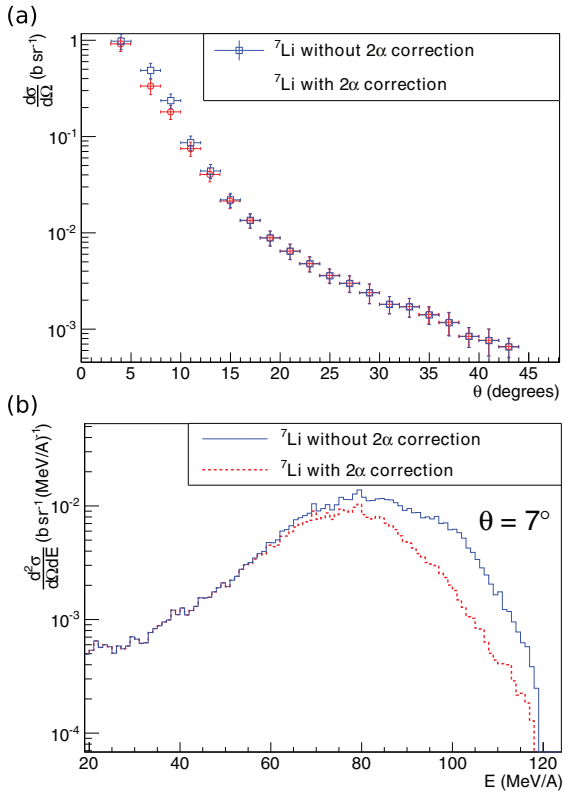

FIG. 5. (Color online) Example of the "2α" pile-up correction for the ^{7}Li distributions. The angular distribution is represented on the left and the energy distribution for $\theta = 7^\circ$ is on the right.

induced by the analysis method. The conclusion of this study is that the systematic errors are too model-dependent to be accurately estimated. To be conservative, the errors obtained at forward angles with the QMD model (which seems to be the closest to experimental data) have been used for all detection angles. Indeed, the identification errors are larger for the higher energies which are mostly detected at forward angles. The systematic errors have thus been overestimated, ranging from 2% to 15% depending on the isotope. To precisely determine these systematic errors, this study will need to be refined with a nuclear model which gives results closer to experimental data.

The systematic error study was realized by combining Monte Carlo simulations and experimental method. The simulation results have shown that the nuclear models available in GEANT4 are not sufficiently accurate to be used to correct the data from detection effects as pile-up or fragmentation in the CsI. Thus, an experimental method using the CsI light shape analysis has been used to correct the distributions of ^{3}He, ^{6}He, ^{6}Li, and ^{7}Li from these effects. Overall, the simulation results were used, in a conservative way, to estimate the error bars on the identification due to the analysis method. The main consequence is a probable overestimation of the error bars in the following results.

IV. EXPERIMENTAL RESULTS

A. Hydrogen and oxygen target cross sections

In order to obtain the double differential cross sections for oxygen and hydrogen, composite targets (CH_2 and Al_2O_3) have been used. The hydrogen cross section has been obtained by combining the cross sections of CH_2 and C targets. The same method has been used to obtain the cross section of oxygen by combining the cross sections of the Al_2O_3 and Al targets as follows:

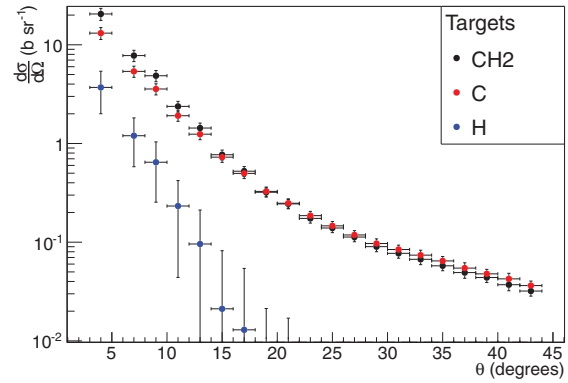

FIG. 6. (Color online) Combination of carbon and CH_2 targets angular distribution to determine the hydrogen angular distribution for α fragments. The angular distribution for the hydrogen target is the difference between both, divided by two.

$$\frac{d\sigma}{d\Omega}(\mathrm{H}) = \frac{1}{2} \times \left(\frac{d\sigma}{d\Omega}(\mathrm{CH_2}) - \frac{d\sigma}{d\Omega}(\mathrm{C}) \right), \quad (2)$$

$$\frac{d\sigma}{d\Omega}(\mathrm{O}) = \frac{1}{3} \times \left(\frac{d\sigma}{d\Omega}(\mathrm{Al_2O_3}) - 2 \times \frac{d\sigma}{d\Omega}(\mathrm{Al}) \right). \quad (3)$$

Figure 6 represents an example of the method used to extract the α angular differential cross sections of hydrogen from CH_2 and C cross sections. A drawback of such a method is that the resulting cross sections are obtained by subtracting the cross sections of the two targets but the uncertainties are the quadratic sum of the uncertainties of the both individual targets. Hydrogen cross sections, which are small compared to carbon cross sections (cf. Fig. 6), have been obtained with larger error bars.

B. Results

All the elements to determine the double differential cross sections are now available. Firstly, the angular distributions will be presented, then, the energy distributions and secondly, the comparison between the real PMMA target and the reconstructed PMMA target cross sections will be shown.

1. Angular distributions

Concerning the angular distributions, all the measurements are represented on the positive angle side. It has to be noted that one measurement out of two in the presented distribution was made at the opposite angle and thus on an other telescope (cf. Fig. 1). All the results for each target (real target or target obtained by composite target reconstruction) are summarized in the appendices (cf. Tables VI–X).

The angular distributions for the carbon target are shown in Fig. 7. One graph per Z is drawn, on which the different

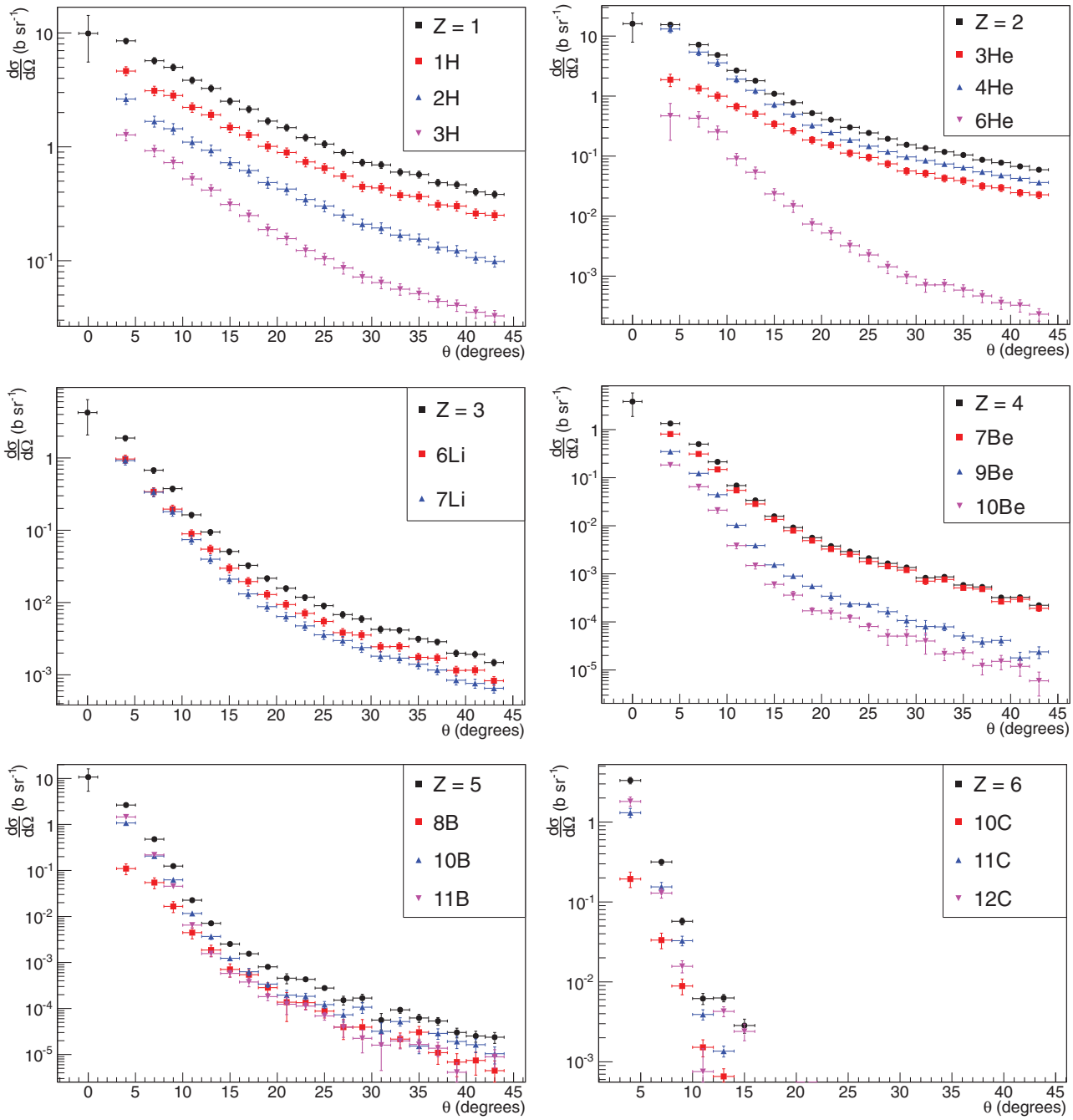

FIG. 7. (Color online) Angular distributions for fragments resulting from the fragmentation on carbon target. Each graph represents the distribution per Z value with the measure at zero degree (except for $Z = 6$ for which fragments are not dissociable from the carbon coming from the beam). The distributions of the different isotopes are superimposed.

detected isotopes and their sum, including a measurement at zero degree angle value, are superimposed.

Regarding zero degree angle value measurements, the normalization versus the number of carbon ions has been done by integrating the number of $Z = 6$ on the ΔE-E matrix. Due to the direct detection of the beam particles, these measurements were done at low beam intensity ($\sim 10^3$ s^{-1}). Moreover, the detection devices were not adapted for zero degree angle measurements and have not permitted a mass identification. This is why the error bars are very large for the zero degree angle value measurements.

It has to be noticed that the production rates are dominated by the hydrogen and helium isotopes with a predominance of α particles at small angles (below 10°) which is compatible with the α cluster structure of the ^{12}C. The results also show an angular emission most forward peaked for heavier fragments. For most of the isotopes, the overall error is of about 5 to 15%, but is dominated by systematic errors that should be reduced

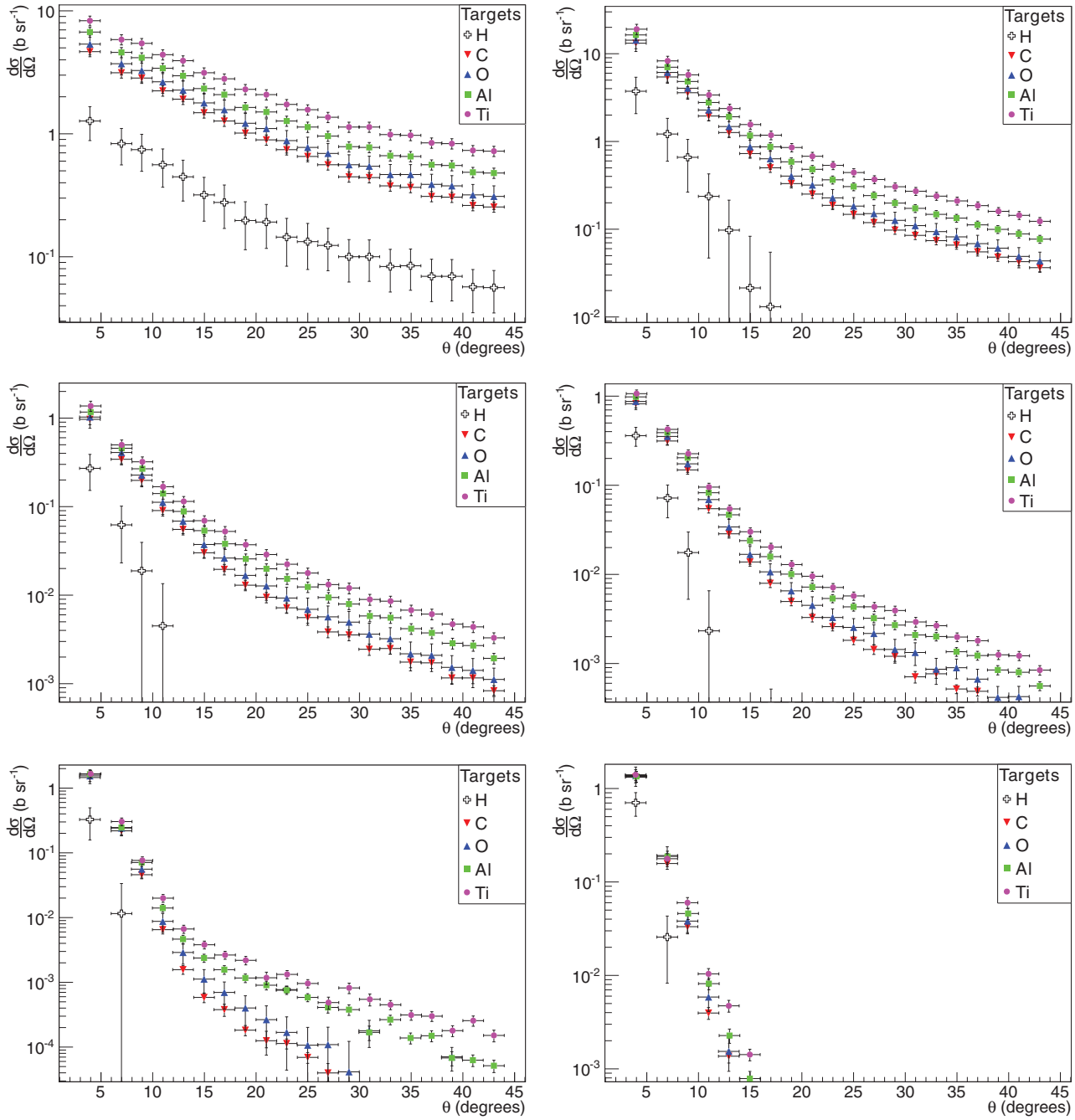

FIG. 8. (Color online) Angular distributions for the most produced fragments of each Z and each elemental targets.

by estimating them with simulations done with more realistic nuclear models (cf. Sec. III).

Figure 8 presents the angular differential cross sections of several isotopes (the most produced of each Z) obtained for the different elemental targets: H, C, O, Al, and ^{nat}Ti.

2. *Production cross sections per isotope*

The angular distributions are in a first approximation well described by a gaussian distribution at forward angles corresponding to fragments emitted by the quasiprojectile. For larger angles, the data are better reproduced by an exponential distribution corresponding to a midrapidity emission. The need for this second component has been observed before by Golovkov and Matsufuji [7,26]. The angular distribution cross sections obtained for all isotopes have been fitted by a function resulting of the sum of a gaussian and an exponential function. The resulting function is described as follows:

$$\frac{d\sigma}{d\Omega} = a \times \exp\left(-\frac{(\theta - b)^2}{2 \cdot c^2}\right) + d \times \exp(e \times |\theta|), \quad (4)$$

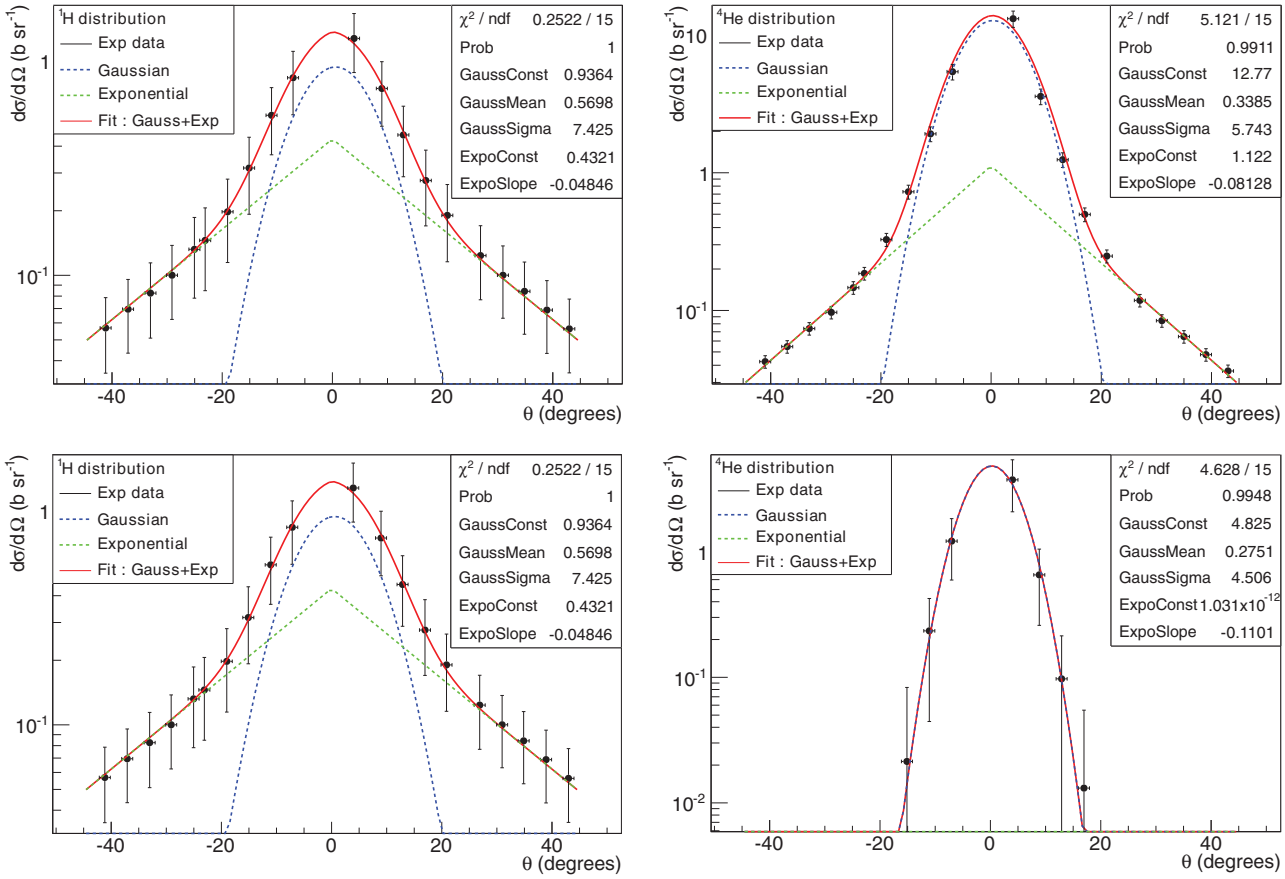

FIG. 9. (Color online) Angular distributions of the protons and α production for the carbon (upper panels) and hydrogen (lower panels) targets. The distributions have been fitted by a sum of a gaussian and an exponential function.

where a, b, c, d, and e are free parameters corresponding, respectively, to the gaussian constant, mean, and σ and to the exponential constant and slope.

Figure 9 represents an example of this fit for proton and α production for the carbon and hydrogen targets. The agreement between the fits and the data is very good for all isotopes and targets. The heavier the fragments are, the more important the contribution of the gaussian term is (quasiprojectile contribution) and the heavier the targets are, the most important the contribution of the exponential term is (midrapidity contribution). It has to be noted that the midrapidity component is not present for $Z > 1$ fragments in the interactions with the hydrogen target.

By integrating the fitted distribution [cf. Eq. (5)], it is then possible to determine the production cross sections of each fragment and and for each target. The results of these integrations are summarized in Table V. Regarding the hydrogen target, it is not possible to integrate the distributions for fragments heavier than ^{7}Be. Indeed, in such cases, the gaussian width become too small to be fitted with our experimental measurements:

$$\sigma = \int_{\Omega} \frac{d\sigma}{d\Omega}\, d\Omega = 2\pi \times \int_{0}^{\pi} \frac{d\sigma}{d\Omega}\, \sin(\theta)\, d\theta. \qquad (5)$$

3. *Energy distributions*

To obtain the double differential cross section, the energy distributions need to be determined at each point of the previous angular distributions. The energies of the fragments are obtained from the energy deposited in the thick silicon stage. The calibration method was made with the KaliVeda toolkit as described previously [18]. The advantage of such a method is that the energy calibration of the nonlinear response for the CsI crystal is not needed, but propagates the error off the thick silicon energy calibration (particularly for low energies in the thick silicon which correspond to high energy protons). The errors made on the energy calibration depend on the nature of the particle. They are summarized in Fig. 10 for several isotopes. They have been estimated from about 20% for 95 MeV protons to ∼3–4% for 95 MeV/nucleon ^{12}C.

Some examples of energy distributions are shown in Figs. 11 and 12. Figure 11 represents ^{4}He and ^{6}Li energy distributions, at different angles for the carbon target. Figure 12 represents ^{4}He and ^{6}Li energy distributions at 4° for different targets.

These distributions are dominated at small angles by a peak centered close to the beam energy (94.6 MeV/nucleon). The energy and amplitude of this peak decrease with the emission angle and the width of this peak decreases with the increasing

TABLE V. Production cross sections per isotope and for each elemental target.

Fragments	σ (barns) Targets				
	H	C	O	Al	Ti
^{1}H	$4.1(0.6) \times 10^{-1}$	1.7(0.1)	2.1(0.2)	3.0(0.2)	4.4(0.3)
^{2}H	$7.3(1.5) \times 10^{-2}$	$7.9(0.4) \times 10^{-1}$	$9.3(0.8) \times 10^{-1}$	1.3(0.1)	1.9(0.1)
^{3}H	$1.6(0.3) \times 10^{-2}$	$3.2(0.2) \times 10^{-1}$	$3.6(0.4) \times 10^{-1}$	$5.2(0.3) \times 10^{-1}$	$7.7(0.4) \times 10^{-1}$
^{3}He	$4.1(0.4) \times 10^{-2}$	$3.3(0.6) \times 10^{-1}$	$4.0(0.5) \times 10^{-1}$	$5.1(0.8) \times 10^{-1}$	$6.7(1.0) \times 10^{-1}$
^{4}He	$2.0(0.8) \times 10^{-1}$	1.2(0.3)	1.2(0.4)	1.7(0.1)	2.0(0.2)
^{6}He	$1.0(0.1) \times 10^{-2}$	$4.9(1.2) \times 10^{-2}$	$5.7(2.2) \times 10^{-2}$	$7.0(1.4) \times 10^{-2}$	$8.7(1.5) \times 10^{-2}$
^{6}Li	$1.2(0.6) \times 10^{-2}$	$6.8(1.1) \times 10^{-2}$	$7.4(1.5) \times 10^{-2}$	$9.4(1.3) \times 10^{-2}$	$1.2(0.2) \times 10^{-1}$
^{7}Li	$8.0(1.8) \times 10^{-3}$	$6.1(1.0) \times 10^{-2}$	$6.6(1.4) \times 10^{-2}$	$8.6(1.3) \times 10^{-2}$	$1.1(0.1) \times 10^{-1}$
^{7}Be	$1.6(0.3) \times 10^{-2}$	$5.0(0.8) \times 10^{-2}$	$5.5(1.0) \times 10^{-2}$	$6.7(1.0) \times 10^{-2}$	$7.6(1.1) \times 10^{-2}$
^{9}Be	–	$1.8(0.7) \times 10^{-2}$	$1.9(0.4) \times 10^{-2}$	$2.3(0.5) \times 10^{-2}$	$3.0(0.5) \times 10^{-2}$
^{10}Be	–	$9.3(2.0) \times 10^{-3}$	$1.0(0.3) \times 10^{-2}$	$1.2(0.3) \times 10^{-2}$	$1.5(0.3) \times 10^{-2}$
^{8}B	–	$6.1(1.8) \times 10^{-3}$	$6.9(2.7) \times 10^{-3}$	$7.8(2.1) \times 10^{-3}$	$8.5(6.3) \times 10^{-3}$
^{10}B	–	$4.7(1.5) \times 10^{-2}$	$5.0(3.3) \times 10^{-2}$	$5.3(1.6) \times 10^{-2}$	$6.2(1.8) \times 10^{-2}$
^{11}B	–	$6.0(2.4) \times 10^{-2}$	$6.3(6.2) \times 10^{-2}$	$6.8(3.9) \times 10^{-2}$	$7.1(2.4) \times 10^{-2}$
^{10}C	–	$8.2(3.0) \times 10^{-3}$	$8.5(5.4) \times 10^{-3}$	$9.3(3.3) \times 10^{-3}$	$1.1(0.4) \times 10^{-2}$
^{11}C	–	$5.3(2.2) \times 10^{-2}$	$5.5(3.7) \times 10^{-2}$	$5.5(2.1) \times 10^{-2}$	$5.8(3.5) \times 10^{-2}$
^{12}C	–	$7.6(4.4) \times 10^{-2}$	$8.1(5.0) \times 10^{-2}$	$8.0(3.9) \times 10^{-2}$	$7.6(3.3) \times 10^{-2}$

mass of the fragments. This observation confirms that most of the detected fragments are coming from the projectile fragmentation.

Concerning the different targets, as for the angular distributions, the cross sections increase with the charge and mass of the target. Moreover, the heavier the target, the higher the cross sections at low energies.

4. PMMA reconstruction

To check the validity of the target cross sections combination method, the results obtained with the PMMA target will be used. The PMMA chemical composition is $C_5H_8O_2$, by combining the obtained carbon, hydrogen and oxygen target cross sections, we should be able to reproduce the cross sections for the PMMA target as follows:

$$\frac{d\sigma}{d\Omega}(\text{PMMA}) = 5 \times \frac{d\sigma}{d\Omega}(\text{C}) + 8 \times \frac{d\sigma}{d\Omega}(\text{H}) + 2 \times \frac{d\sigma}{d\Omega}(\text{O}). \tag{6}$$

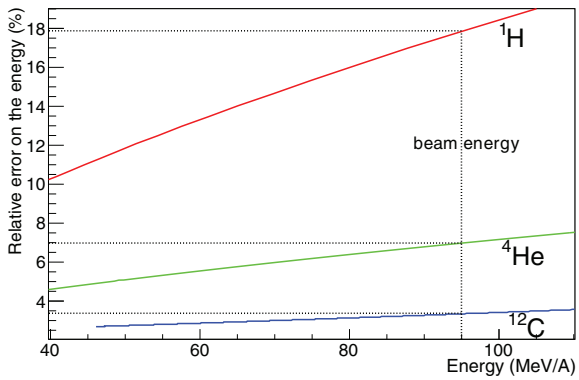

FIG. 10. (Color online) Estimated errors on the energy due to the calibration method used with the thick silicon detector.

Comparisons between the cross sections measured with the PMMA target and the calculated ones from elemental target cross sections are shown in Fig. 13. On the left-hand side are represented the angular distributions for protons, ^{4}He and

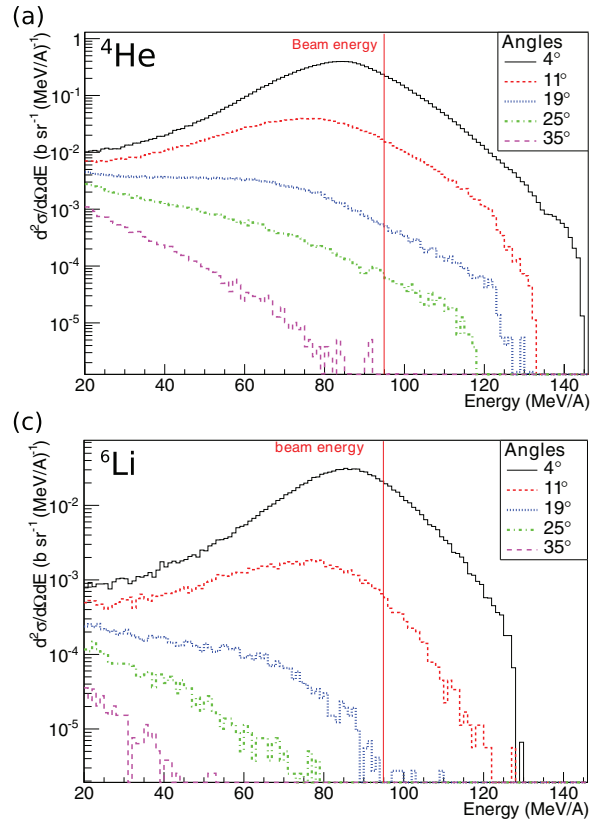

FIG. 11. (Color online) ^{4}He (a) and ^{6}Li (b) energy distributions at different angles for the carbon target.

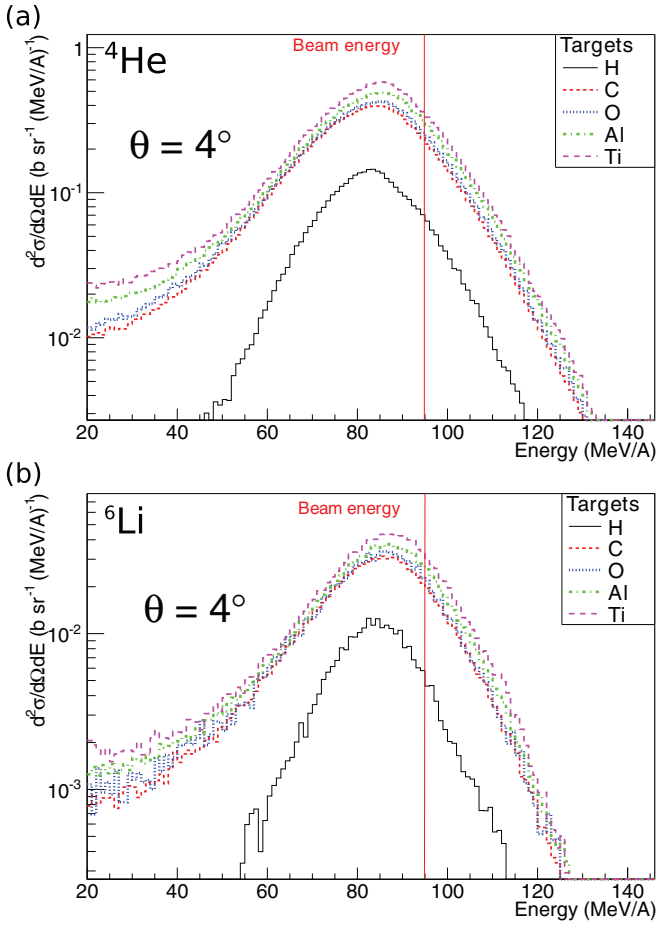

FIG. 12. (Color online) ^{4}He (a) and ^{6}Li (b) energy distributions for different targets at 4°.

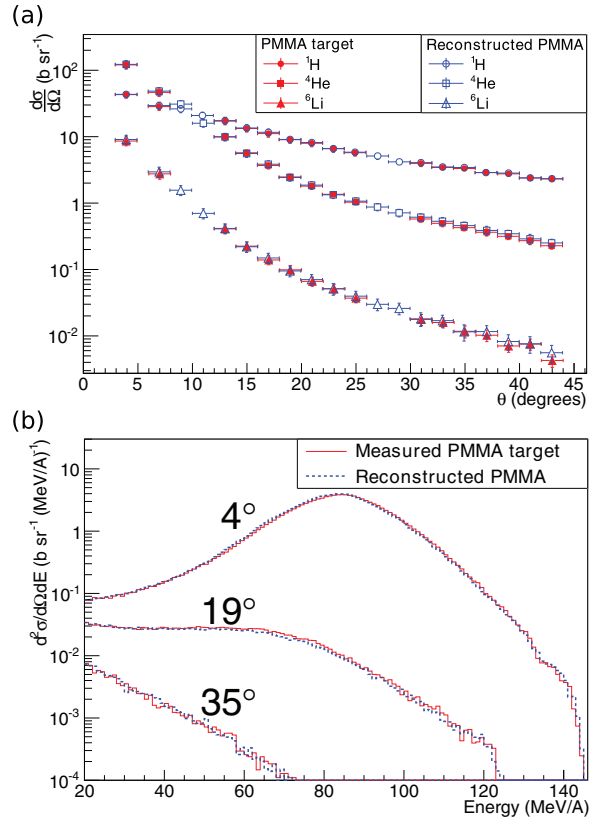

FIG. 13. (Color online) Comparisons of the differential cross sections for the PMMA target and the reconstructed PMMA target for different isotopes (a) and ^{4}He energy distributions at different angles (b).

^{6}Li fragments. On the right-hand side are represented the ^{4}He energy distributions at 4, 19, and 35°. The data at 9, 11, 27, and 39° are missing for the PMMA target, explaining the holes in the PMMA angular distributions.

The results between the real target and the reconstructed one are very close to each other. The agreement between these two targets is about 1 to 5% both for angular and energy distributions.

This last result confirms that the data are of good quality and overall, validate the target combination method. Thus, with the cross sections presented in this article, most of the human organic tissues cross sections can be reproduced at 95 MeV/nucleon.

V. CONCLUSION

Measurements for 20 different angles and five different targets led to the double differential fragmentation cross sections of ^{12}C on hydrogen, carbon, oxygen, aluminum, and titanium in fragmented particles, ranging from protons to carbon ion isotopes.

The angular distributions are dominated by the emission of light fragments ($Z < 3$), more especially by α particles at forward angles, which is consistent with the α cluster structure of the ^{12}C ion. These results are in agreement with previous experiments with thick targets [12] and at lower energies [5]. The production rates and the emission angles are increasing when the charge and mass of the target are increasing.

Energy distributions are dominated at low angles by a peak close to the beam energy, while the amplitude and energy mean value of the peak decrease when the angle of emission increases. The production of low energy particles increases with the target charge and mass. These observations indicate that most of the emitted particles result from the projectile fragmentation during nuclear reactions.

The presented experimental results will contribute directly to constrain the nuclear reaction models used in different Monte Carlo simulation toolkits as GEANT4 or FLUKA.

Moreover, the method used to combine the cross sections of composite targets to extract an elemental target (CH_2 and C to extract H) has been validated. By comparing the double differential cross sections of the real PMMA target with the one of the reconstructed PMMA target (result of combination of Al_2O_3, Al, CH_2, and C target), it gives us the information that most of the human body tissue cross sections are reproducible using this method.

In order to complete these data, new measurements at zero degree for the different thin targets are planned.

All the experimental results including all angular and energy distributions for each target are in free access on the website http://hadrontherapy-data.in2p3.fr.

APPENDIX A: CROSS SECTION FOR THE HYDROGEN TARGET

TABLE VI. ^{12}C fragmentation cross sections for the hydrogen target at different angles. The values in parentheses represent the uncertainties [4.55(0.52) is equivalent to 4.55 ± 0.52].

θ (deg)	^{1}H $d\sigma/d\Omega$ (b sr^{-1})	^{2}H $d\sigma/d\Omega$ (b sr^{-1})	^{3}H $d\sigma/d\Omega$ (b sr^{-1})	^{3}He $d\sigma/d\Omega$ (b sr^{-1})	^{4}He $d\sigma/d\Omega$ (b sr^{-1})	^{6}He $d\sigma/d\Omega$ (b sr^{-1})
4(1)	1.26(0.39)	$4.3(2.3) \times 10^{-1}$	$1.6(1.1) \times 10^{-1}$	$4.5(4.0) \times 10^{-1}$	3.7(1.7)	$1.6(3.0) \times 10^{-1}$
7(1)	$8.3(2.7) \times 10^{-1}$	$2.6(1.5) \times 10^{-1}$	$1.09(0.85) \times 10^{-1}$	$2.8(2.0) \times 10^{-1}$	1.20(0.62)	$8.66(11.0) \times 10^{-2}$
9(1)	$7.4(2.5) \times 10^{-1}$	$2.2(1.3) \times 10^{-1}$	$7.4(6.5) \times 10^{-2}$	$1.9(1.5) \times 10^{-1}$	$6.5(4.0) \times 10^{-1}$	$3.2(5.2) \times 10^{-2}$
11(1)	$5.6(1.9) \times 10^{-1}$	$1.47(0.97) \times 10^{-1}$	$4.4(4.6) \times 10^{-2}$	$1.04(0.82) \times 10^{-1}$	$2.3(1.9) \times 10^{-1}$	$3.7(15.0) \times 10^{-3}$
13(1)	$4.5(1.6) \times 10^{-1}$	$1.12(0.81) \times 10^{-1}$	$2.5(3.6) \times 10^{-2}$	$5.9(5.8) \times 10^{-2}$	$9.61(12.0) \times 10^{-2}$	$1.1(8.6) \times 10^{-3}$
15(1)	$3.1(1.2) \times 10^{-1}$	$8.1(6.3) \times 10^{-2}$	$1.1(2.6) \times 10^{-2}$	$2.9(3.7) \times 10^{-2}$	$2.1(6.2) \times 10^{-2}$	–
17(1)	$2.7(1.1) \times 10^{-1}$	$7.6(5.4) \times 10^{-2}$	$9.33(21.0) \times 10^{-3}$	$2.1(2.8) \times 10^{-2}$	$1.3(4.2) \times 10^{-2}$	–
19(1)	$1.96(0.83) \times 10^{-1}$	$5.3(4.2) \times 10^{-2}$	$2.4(15.0) \times 10^{-3}$	$7.44(19.0) \times 10^{-3}$	–	–
21(1)	$1.90(0.75) \times 10^{-1}$	$5.0(3.7) \times 10^{-2}$	$1.94(13.0) \times 10^{-3}$	$5.08(15.0) \times 10^{-3}$	–	–
23(1)	$1.44(0.61) \times 10^{-1}$	$3.4(2.9) \times 10^{-2}$	–	–	–	–
27(1)	$1.23(0.47) \times 10^{-1}$	$2.5(2.1) \times 10^{-2}$	–	–	–	–
31(1)	$9.9(3.7) \times 10^{-2}$	$1.4(1.6) \times 10^{-2}$	–	–	–	–
35(1)	$8.4(3.1) \times 10^{-2}$	$1.0(1.3) \times 10^{-2}$	–	–	–	–
39(1)	$6.9(2.6) \times 10^{-2}$	–	–	–	–	–

θ (deg)	^{6}Li $d\sigma/d\Omega$ (b sr^{-1})	^{7}Li $d\sigma/d\Omega$ (b sr^{-1})	^{7}Be $d\sigma/d\Omega$ (b sr^{-1})	^{9}Be $d\sigma/d\Omega$ (b sr^{-1})	^{10}Be $d\sigma/d\Omega$ (b sr^{-1})	^{8}B $d\sigma/d\Omega$ (b sr^{-1})
4(1)	$2.7(1.2) \times 10^{-1}$	$1.8(1.0) \times 10^{-1}$	$3.59(0.86) \times 10^{-1}$	$6.4(3.1) \times 10^{-2}$	$1.9(1.9) \times 10^{-2}$	$3.5(2.8) \times 10^{-2}$
7(1)	$6.2(3.9) \times 10^{-2}$	$4.4(3.7) \times 10^{-2}$	$7.2(2.9) \times 10^{-2}$	$1.5(1.1) \times 10^{-2}$	$5.2(6.8) \times 10^{-3}$	$8.25(12.0) \times 10^{-3}$
9(1)	$1.9(2.1) \times 10^{-2}$	$9.65(18.0) \times 10^{-3}$	$1.8(1.2) \times 10^{-2}$	$1.7(3.6) \times 10^{-3}$	–	–
11(1)	$4.4(9.0) \times 10^{-3}$	$1.0(7.2) \times 10^{-3}$	$2.3(4.2) \times 10^{-3}$	$2.7(8.4) \times 10^{-4}$	–	–

θ (deg)	^{10}B $d\sigma/d\Omega$ (b sr^{-1})	^{11}B $d\sigma/d\Omega$ (b sr^{-1})	^{10}C $d\sigma/d\Omega$ (b sr^{-1})	^{11}C $d\sigma/d\Omega$ (b sr^{-1})	^{12}C $d\sigma/d\Omega$ (b sr^{-1})
4(1)	$4.1(1.4) \times 10^{-1}$	$3.2(1.7) \times 10^{-1}$	$1.06(0.49) \times 10^{-1}$	$7.0(2.0) \times 10^{-1}$	$2.0(1.9) \times 10^{-1}$
7(1)	$3.5(2.3) \times 10^{-2}$	$1.1(2.2) \times 10^{-2}$	$7.5(6.5) \times 10^{-3}$	$2.6(1.7) \times 10^{-2}$	–
9(1)	–	–	–	–	–

APPENDIX B: CROSS SECTION FOR THE CARBON TARGET

TABLE VII. ^{12}C fragmentation cross sections for the carbon target at different angles. The values in parentheses represent the uncertainties [4.55(0.52) is equivalent to 4.55 ± 0.52].

θ (deg)	^{1}H $d\sigma/d\Omega$ (b sr^{-1})	^{2}H $d\sigma/d\Omega$ (b sr^{-1})	^{3}H $d\sigma/d\Omega$ (b sr^{-1})	^{3}He $d\sigma/d\Omega$ (b sr^{-1})	^{4}He $d\sigma/d\Omega$ (b sr^{-1})	^{6}He $d\sigma/d\Omega$ (b sr^{-1})
4(1)	4.63(0.42)	2.63(0.28)	1.27(0.14)	1.88(0.44)	$1.32(0.18) \times 10^{1}$	$4.7(2.9) \times 10^{-1}$
7(1)	3.11(0.30)	1.67(0.18)	$9.2(1.1) \times 10^{-1}$	1.34(0.23)	5.42(0.70)	$4.3(1.2) \times 10^{-1}$
9(1)	2.82(0.27)	1.44(0.16)	$7.27(0.84) \times 10^{-1}$	$10.0(1.7) \times 10^{-1}$	3.59(0.47)	$2.53(0.64) \times 10^{-1}$
11(1)	2.22(0.21)	1.10(0.12)	$5.23(0.60) \times 10^{-1}$	$6.7(1.0) \times 10^{-1}$	1.92(0.24)	$9.0(2.1) \times 10^{-2}$
13(1)	1.91(0.18)	$9.3(1.0) \times 10^{-1}$	$4.17(0.48) \times 10^{-1}$	$5.03(0.73) \times 10^{-1}$	1.24(0.15)	$5.4(1.2) \times 10^{-2}$
15(1)	1.48(0.14)	$7.25(0.79) \times 10^{-1}$	$3.12(0.36) \times 10^{-1}$	$3.42(0.48) \times 10^{-1}$	$7.28(0.85) \times 10^{-1}$	$2.35(0.52) \times 10^{-2}$
17(1)	1.27(0.12)	$6.19(0.68) \times 10^{-1}$	$2.49(0.29) \times 10^{-1}$	$2.64(0.36) \times 10^{-1}$	$4.98(0.57) \times 10^{-1}$	$1.48(0.33) \times 10^{-2}$
19(1)	1.01(0.097)	$4.86(0.53) \times 10^{-1}$	$1.88(0.22) \times 10^{-1}$	$1.86(0.25) \times 10^{-1}$	$3.27(0.36) \times 10^{-1}$	$7.4(1.6) \times 10^{-3}$
21(1)	$8.92(0.86) \times 10^{-1}$	$4.26(0.47) \times 10^{-1}$	$1.56(0.18) \times 10^{-1}$	$1.52(0.21) \times 10^{-1}$	$2.48(0.27) \times 10^{-1}$	$5.2(1.2) \times 10^{-3}$
23(1)	$7.37(0.71) \times 10^{-1}$	$3.45(0.38) \times 10^{-1}$	$1.23(0.14) \times 10^{-1}$	$1.12(0.15) \times 10^{-1}$	$1.86(0.20) \times 10^{-1}$	$3.22(0.71) \times 10^{-3}$
27(1)	$5.53(0.53) \times 10^{-1}$	$2.52(0.28) \times 10^{-1}$	$8.6(1.0) \times 10^{-2}$	$7.4(1.0) \times 10^{-2}$	$1.18(0.12) \times 10^{-1}$	$1.43(0.33) \times 10^{-3}$
31(1)	$4.36(0.42) \times 10^{-1}$	$1.94(0.21) \times 10^{-1}$	$6.42(0.74) \times 10^{-2}$	$5.14(0.70) \times 10^{-2}$	$8.43(0.88) \times 10^{-2}$	$7.1(1.7) \times 10^{-4}$
35(1)	$3.66(0.35) \times 10^{-1}$	$1.55(0.17) \times 10^{-1}$	$5.14(0.59) \times 10^{-2}$	$3.92(0.53) \times 10^{-2}$	$6.46(0.67) \times 10^{-2}$	$5.8(1.3) \times 10^{-4}$
39(1)	$3.02(0.29) \times 10^{-1}$	$1.22(0.13) \times 10^{-1}$	$4.05(0.47) \times 10^{-2}$	$2.96(0.40) \times 10^{-2}$	$4.78(0.50) \times 10^{-2}$	$3.61(0.82) \times 10^{-4}$

θ (deg)	^{6}Li $d\sigma/d\Omega$ (b sr^{-1})	^{7}Li $d\sigma/d\Omega$ (b sr^{-1})	^{7}Be $d\sigma/d\Omega$ (b sr^{-1})	^{9}Be $d\sigma/d\Omega$ (b sr^{-1})	^{10}Be $d\sigma/d\Omega$ (b sr^{-1})	^{8}B $d\sigma/d\Omega$ (b sr^{-1})
4(1)	$9.7(1.3) \times 10^{-1}$	$9.2(1.2) \times 10^{-1}$	$8.09(0.81) \times 10^{-1}$	$3.50(0.37) \times 10^{-1}$	$1.84(0.24) \times 10^{-1}$	$1.10(0.29) \times 10^{-1}$
7(1)	$3.41(0.46) \times 10^{-1}$	$3.36(0.45) \times 10^{-1}$	$3.12(0.32) \times 10^{-1}$	$1.23(0.14) \times 10^{-1}$	$6.49(0.88) \times 10^{-2}$	$5.5(1.5) \times 10^{-2}$
9(1)	$1.96(0.27) \times 10^{-1}$	$1.81(0.24) \times 10^{-1}$	$1.48(0.15) \times 10^{-1}$	$4.44(0.49) \times 10^{-2}$	$2.11(0.29) \times 10^{-2}$	$1.66(0.45) \times 10^{-2}$
11(1)	$8.9(1.2) \times 10^{-2}$	$7.4(1.0) \times 10^{-2}$	$5.46(0.57) \times 10^{-2}$	$1.03(0.12) \times 10^{-2}$	$3.87(0.56) \times 10^{-3}$	$4.5(1.2) \times 10^{-3}$
13(1)	$5.47(0.74) \times 10^{-2}$	$3.98(0.54) \times 10^{-2}$	$2.84(0.30) \times 10^{-2}$	$3.89(0.46) \times 10^{-3}$	$1.49(0.23) \times 10^{-3}$	$1.87(0.51) \times 10^{-3}$
15(1)	$2.98(0.40) \times 10^{-2}$	$2.10(0.29) \times 10^{-2}$	$1.36(0.14) \times 10^{-2}$	$1.54(0.18) \times 10^{-3}$	$6.04(0.86) \times 10^{-4}$	$7.1(2.3) \times 10^{-4}$
17(1)	$1.95(0.26) \times 10^{-2}$	$1.32(0.18) \times 10^{-2}$	$7.92(0.84) \times 10^{-3}$	$9.0(1.2) \times 10^{-4}$	$3.60(0.73) \times 10^{-4}$	$5.4(1.6) \times 10^{-4}$
19(1)	$1.29(0.18) \times 10^{-2}$	$8.8(1.2) \times 10^{-3}$	$4.92(0.52) \times 10^{-3}$	$5.54(0.66) \times 10^{-4}$	$1.70(0.28) \times 10^{-4}$	$2.84(0.78) \times 10^{-4}$
21(1)	$9.4(1.3) \times 10^{-3}$	$6.40(0.87) \times 10^{-3}$	$3.28(0.36) \times 10^{-3}$	$3.42(0.60) \times 10^{-4}$	$1.54(0.40) \times 10^{-4}$	$1.37(0.85) \times 10^{-4}$
23(1)	$7.08(0.96) \times 10^{-3}$	$4.75(0.65) \times 10^{-3}$	$2.55(0.27) \times 10^{-3}$	$2.36(0.32) \times 10^{-4}$	$1.20(0.21) \times 10^{-4}$	$1.34(0.38) \times 10^{-4}$
27(1)	$3.83(0.54) \times 10^{-3}$	$2.98(0.42) \times 10^{-3}$	$1.43(0.17) \times 10^{-3}$	$1.63(0.35) \times 10^{-4}$	$5.1(1.8) \times 10^{-5}$	$3.9(1.8) \times 10^{-5}$
31(1)	$2.44(0.36) \times 10^{-3}$	$1.81(0.27) \times 10^{-3}$	$7.0(1.0) \times 10^{-4}$	$8.0(2.7) \times 10^{-5}$	$4.0(1.9) \times 10^{-5}$	$8.0(8.3) \times 10^{-6}$
35(1)	$1.74(0.24) \times 10^{-3}$	$1.40(0.19) \times 10^{-3}$	$5.11(0.59) \times 10^{-4}$	$5.08(0.98) \times 10^{-5}$	$2.29(0.62) \times 10^{-5}$	$3.0(1.0) \times 10^{-5}$
39(1)	$1.15(0.16) \times 10^{-3}$	$8.4(1.2) \times 10^{-4}$	$2.65(0.33) \times 10^{-4}$	$4.11(0.88) \times 10^{-5}$	$1.51(0.50) \times 10^{-5}$	$6.8(3.6) \times 10^{-6}$

θ (deg)	^{10}B $d\sigma/d\Omega$ (b sr^{-1})	^{11}B $d\sigma/d\Omega$ (b sr^{-1})	^{10}C $d\sigma/d\Omega$ (b sr^{-1})	^{11}C $d\sigma/d\Omega$ (b sr^{-1})	^{12}C $d\sigma/d\Omega$ (b sr^{-1})
4(1)	1.08(0.14)	1.45(0.19)	$1.94(0.42) \times 10^{-1}$	1.31(0.17)	1.81(0.25)
7(1)	$2.06(0.28) \times 10^{-1}$	$2.18(0.30) \times 10^{-1}$	$3.34(0.74) \times 10^{-2}$	$1.54(0.21) \times 10^{-1}$	$1.29(0.18) \times 10^{-1}$
9(1)	$6.25(0.85) \times 10^{-2}$	$4.55(0.62) \times 10^{-2}$	$8.9(2.0) \times 10^{-3}$	$3.28(0.45) \times 10^{-2}$	$1.57(0.27) \times 10^{-2}$
11(1)	$1.16(0.16) \times 10^{-2}$	$6.50(0.92) \times 10^{-3}$	$1.52(0.37) \times 10^{-3}$	$3.91(0.57) \times 10^{-3}$	$7.5(7.1) \times 10^{-4}$
13(1)	$3.68(0.53) \times 10^{-3}$	$1.56(0.24) \times 10^{-3}$	$6.6(1.6) \times 10^{-4}$	$1.36(0.21) \times 10^{-3}$	–
15(1)	$1.24(0.17) \times 10^{-3}$	$5.79(0.99) \times 10^{-4}$	$1.96(0.46) \times 10^{-4}$	$2.50(0.61) \times 10^{-4}$	–
17(1)	$6.3(1.2) \times 10^{-4}$	$3.77(0.81) \times 10^{-4}$	$2.95.0(10.0) \times 10^{-5}$	$1.06(0.88) \times 10^{-4}$	–
19(1)	$3.40(0.52) \times 10^{-4}$	$1.81(0.33) \times 10^{-4}$	$4.2(1.2) \times 10^{-5}$	$8.0(1.5) \times 10^{-5}$	–
21(1)	$1.95(0.53) \times 10^{-4}$	$1.24(0.50) \times 10^{-4}$	$4.7(3.6) \times 10^{-5}$	$3.8(3.0) \times 10^{-5}$	–
23(1)	$1.84(0.30) \times 10^{-4}$	$1.13(0.20) \times 10^{-4}$	$1.19(0.49) \times 10^{-5}$	$3.42(0.85) \times 10^{-5}$	–
27(1)	$7.3(2.3) \times 10^{-5}$	$3.9(1.6) \times 10^{-5}$	–	$1.7(1.0) \times 10^{-5}$	–
31(1)	$3.2(1.7) \times 10^{-5}$	$1.6(1.2) \times 10^{-5}$	–	–	–
35(1)	$1.53(0.49) \times 10^{-5}$	$1.65(0.51) \times 10^{-5}$	–	–	–
39(1)	$1.92(0.58) \times 10^{-5}$	$4.1(2.4) \times 10^{-6}$	–	–	–

APPENDIX C: CROSS SECTION FOR THE OXYGEN TARGET

TABLE VIII. ^{12}C fragmentation cross sections for the oxygen target at different angles. The values in parentheses represent the uncertainties [4.55(0.52) is equivalent to 4.55 ± 0.52].

θ (deg)	^{1}H $d\sigma/d\Omega$ (b sr^{-1})	^{2}H $d\sigma/d\Omega$ (b sr^{-1})	^{3}H $d\sigma/d\Omega$ (b sr^{-1})	^{3}He $d\sigma/d\Omega$ (b sr^{-1})	^{4}He $d\sigma/d\Omega$ (b sr^{-1})	^{6}He $d\sigma/d\Omega$ (b sr^{-1})
4(1)	5.33(0.98)	2.99(0.64)	1.41(0.32)	2.11(0.92)	$1.41(0.37) \times 10^{1}$	$4.9(5.8) \times 10^{-1}$
7(1)	3.68(0.71)	1.93(0.43)	1.02(0.24)	1.53(0.52)	6.0(1.5)	$4.9(2.5) \times 10^{-1}$
9(1)	3.27(0.64)	1.70(0.38)	$8.4(2.0) \times 10^{-1}$	1.16(0.38)	4.0(1.0)	$2.9(1.4) \times 10^{-1}$
11(1)	2.64(0.52)	1.31(0.30)	$6.2(1.5) \times 10^{-1}$	$8.0(2.4) \times 10^{-1}$	2.24(0.55)	$1.10(0.50) \times 10^{-1}$
13(1)	2.25(0.45)	1.12(0.25)	$5.0(1.2) \times 10^{-1}$	$6.0(1.8) \times 10^{-1}$	1.46(0.37)	$6.5(3.1) \times 10^{-2}$
15(1)	1.78(0.35)	$8.6(2.0) \times 10^{-1}$	$3.69(0.90) \times 10^{-1}$	$4.1(1.2) \times 10^{-1}$	$8.7(2.1) \times 10^{-1}$	$3.0(1.4) \times 10^{-2}$
17(1)	1.55(0.31)	$7.6(1.7) \times 10^{-1}$	$3.07(0.76) \times 10^{-1}$	$3.28(0.94) \times 10^{-1}$	$6.3(1.5) \times 10^{-1}$	$2.02(0.96) \times 10^{-2}$
19(1)	1.21(0.25)	$5.8(1.4) \times 10^{-1}$	$2.23(0.56) \times 10^{-1}$	$2.25(0.64) \times 10^{-1}$	$4.02(0.96) \times 10^{-1}$	$9.7(4.9) \times 10^{-3}$
21(1)	1.09(0.22)	$5.2(1.2) \times 10^{-1}$	$1.90(0.48) \times 10^{-1}$	$1.91(0.55) \times 10^{-1}$	$3.16(0.77) \times 10^{-1}$	$6.5(3.6) \times 10^{-3}$
23(1)	$8.7(1.8) \times 10^{-1}$	$4.02(0.97) \times 10^{-1}$	$1.43(0.37) \times 10^{-1}$	$1.33(0.39) \times 10^{-1}$	$2.25(0.56) \times 10^{-1}$	$4.0(2.3) \times 10^{-3}$
27(1)	$6.8(1.4) \times 10^{-1}$	$3.11(0.73) \times 10^{-1}$	$1.05(0.27) \times 10^{-1}$	$9.3(2.6) \times 10^{-2}$	$1.49(0.36) \times 10^{-1}$	$2.2(1.1) \times 10^{-3}$
31(1)	$5.4(1.1) \times 10^{-1}$	$2.34(0.56) \times 10^{-1}$	$7.5(2.0) \times 10^{-2}$	$6.3(1.9) \times 10^{-2}$	$1.09(0.26) \times 10^{-1}$	$6.1(5.9) \times 10^{-4}$
35(1)	$4.60(0.95) \times 10^{-1}$	$1.92(0.45) \times 10^{-1}$	$6.0(1.5) \times 10^{-2}$	$4.7(1.4) \times 10^{-2}$	$8.1(2.0) \times 10^{-2}$	$6.9(4.2) \times 10^{-4}$
39(1)	$3.76(0.80) \times 10^{-1}$	$1.50(0.36) \times 10^{-1}$	$4.6(1.2) \times 10^{-2}$	$3.6(1.0) \times 10^{-2}$	$6.0(1.5) \times 10^{-2}$	$5.1(2.8) \times 10^{-4}$
θ (deg)	^{6}Li $d\sigma/d\Omega$ (b sr^{-1})	^{7}Li $d\sigma/d\Omega$ (b sr^{-1})	^{7}Be $d\sigma/d\Omega$ (b sr^{-1})	^{9}Be $d\sigma/d\Omega$ (b sr^{-1})	^{10}Be $d\sigma/d\Omega$ (b sr^{-1})	^{8}B $d\sigma/d\Omega$ (b sr^{-1})
4(1)	1.02(0.26)	$9.8(2.5) \times 10^{-1}$	$8.7(1.6) \times 10^{-1}$	$3.59(0.73) \times 10^{-1}$	$1.97(0.50) \times 10^{-1}$	$1.16(0.59) \times 10^{-1}$
7(1)	$4.0(1.0) \times 10^{-1}$	$3.8(1.0) \times 10^{-1}$	$3.51(0.69) \times 10^{-1}$	$1.53(0.30) \times 10^{-1}$	$7.5(1.8) \times 10^{-2}$	$6.4(3.1) \times 10^{-2}$
9(1)	$2.24(0.60) \times 10^{-1}$	$2.06(0.56) \times 10^{-1}$	$1.71(0.35) \times 10^{-1}$	$5.3(1.1) \times 10^{-2}$	$2.49(0.68) \times 10^{-2}$	$2.0(1.1) \times 10^{-2}$
11(1)	$1.10(0.30) \times 10^{-1}$	$9.3(2.6) \times 10^{-2}$	$6.9(1.4) \times 10^{-2}$	$1.35(0.32) \times 10^{-2}$	$5.5(1.7) \times 10^{-3}$	$5.3(3.1) \times 10^{-3}$
13(1)	$6.8(1.9) \times 10^{-2}$	$5.0(1.5) \times 10^{-2}$	$3.36(0.75) \times 10^{-2}$	$5.4(1.5) \times 10^{-3}$	$1.72(0.69) \times 10^{-3}$	$2.6(1.5) \times 10^{-3}$
15(1)	$3.7(1.1) \times 10^{-2}$	$2.72(0.85) \times 10^{-2}$	$1.67(0.38) \times 10^{-2}$	$2.73(0.67) \times 10^{-3}$	$8.4(3.3) \times 10^{-4}$	$9.1(6.8) \times 10^{-4}$
17(1)	$2.59(0.78) \times 10^{-2}$	$1.72(0.57) \times 10^{-2}$	$1.05(0.25) \times 10^{-2}$	$1.20(0.43) \times 10^{-3}$	$6.0(2.5) \times 10^{-4}$	$6.8(4.5) \times 10^{-4}$
19(1)	$1.64(0.51) \times 10^{-2}$	$1.15(0.39) \times 10^{-2}$	$6.5(1.5) \times 10^{-3}$	$8.2(2.8) \times 10^{-4}$	$4.2(1.7) \times 10^{-4}$	$3.9(2.9) \times 10^{-4}$
21(1)	$1.27(0.40) \times 10^{-2}$	$9.0(3.0) \times 10^{-3}$	$4.4(1.1) \times 10^{-3}$	$5.1(2.4) \times 10^{-4}$	$3.7(1.4) \times 10^{-4}$	$2.4(2.1) \times 10^{-4}$
23(1)	$9.2(3.0) \times 10^{-3}$	$6.2(2.3) \times 10^{-3}$	$3.27(0.82) \times 10^{-3}$	$4.5(1.7) \times 10^{-4}$	$2.0(1.1) \times 10^{-4}$	$1.9(1.3) \times 10^{-4}$
27(1)	$5.6(1.9) \times 10^{-3}$	$3.5(1.4) \times 10^{-3}$	$2.16(0.55) \times 10^{-3}$	$2.6(1.4) \times 10^{-4}$	–	$1.33(0.74) \times 10^{-4}$
31(1)	$3.6(1.2) \times 10^{-3}$	$2.5(1.0) \times 10^{-3}$	$1.31(0.38) \times 10^{-3}$	$1.6(1.1) \times 10^{-4}$	–	$7.32(51.0) \times 10^{-6}$
35(1)	$2.15(0.78) \times 10^{-3}$	$2.29(0.72) \times 10^{-3}$	$8.9(2.2) \times 10^{-4}$	$1.31(0.53) \times 10^{-4}$	–	$4.8(2.9) \times 10^{-5}$
39(1)	$1.51(0.55) \times 10^{-3}$	$1.19(0.49) \times 10^{-3}$	$4.1(1.4) \times 10^{-4}$	$1.39(0.44) \times 10^{-4}$	–	$1.2(1.7) \times 10^{-5}$
θ (deg)	^{10}B $d\sigma/d\Omega$ (b sr^{-1})	^{11}B $d\sigma/d\Omega$ (b sr^{-1})	^{10}C $d\sigma/d\Omega$ (b sr^{-1})	^{11}C $d\sigma/d\Omega$ (b sr^{-1})	^{12}C $d\sigma/d\Omega$ (b sr^{-1})	
4(1)	1.12(0.27)	1.52(0.37)	$1.96(0.80) \times 10^{-1}$	1.36(0.32)	1.92(0.47)	
7(1)	$2.59(0.64) \times 10^{-1}$	$2.39(0.59) \times 10^{-1}$	$4.3(1.8) \times 10^{-2}$	$1.91(0.46) \times 10^{-1}$	$1.52(0.38) \times 10^{-1}$	
9(1)	$7.2(1.9) \times 10^{-2}$	$5.6(1.5) \times 10^{-2}$	$9.9(4.4) \times 10^{-3}$	$3.8(1.0) \times 10^{-2}$	$2.12(0.72) \times 10^{-2}$	
11(1)	$1.66(0.47) \times 10^{-2}$	$8.6(2.8) \times 10^{-3}$	$2.04(0.99) \times 10^{-3}$	$5.8(1.8) \times 10^{-3}$	$2.5(1.3) \times 10^{-3}$	
13(1)	$5.5(1.8) \times 10^{-3}$	$2.86(0.99) \times 10^{-3}$	$7.8(4.3) \times 10^{-4}$	–	–	
15(1)	$1.70(0.66) \times 10^{-3}$	–	–	–	–	

APPENDIX D: CROSS SECTION FOR THE ALUMINUM TARGET

TABLE IX. ^{12}C fragmentation cross sections for the aluminum target at different angles. The values in parentheses represent the uncertainties [4.55(0.52) is equivalent to 4.55 ± 0.52].

θ (deg)	^{1}H $d\sigma/d\Omega$ (b sr^{-1})	^{2}H $d\sigma/d\Omega$ (b sr^{-1})	^{3}H $d\sigma/d\Omega$ (b sr^{-1})	^{3}He $d\sigma/d\Omega$ (b sr^{-1})	^{4}He $d\sigma/d\Omega$ (b sr^{-1})	^{6}He $d\sigma/d\Omega$ (b sr^{-1})
4(1)	6.68(0.61)	3.80(0.40)	1.83(0.20)	2.54(0.56)	$1.63(0.22) \times 10^{1}$	$5.6(3.5) \times 10^{-1}$
7(1)	4.54(0.44)	2.49(0.27)	1.35(0.15)	1.88(0.31)	6.93(0.90)	$5.4(1.5) \times 10^{-1}$
9(1)	4.15(0.40)	2.20(0.24)	1.11(0.13)	1.43(0.23)	4.76(0.62)	$3.43(0.86) \times 10^{-1}$
11(1)	3.38(0.33)	1.71(0.19)	$8.20(0.94) \times 10^{-1}$	$9.9(1.5) \times 10^{-1}$	2.75(0.34)	$1.38(0.31) \times 10^{-1}$
13(1)	2.94(0.28)	1.49(0.16)	$6.80(0.78) \times 10^{-1}$	$7.8(1.1) \times 10^{-1}$	1.89(0.23)	$8.9(2.0) \times 10^{-2}$
15(1)	2.33(0.22)	1.16(0.13)	$5.10(0.59) \times 10^{-1}$	$5.31(0.74) \times 10^{-1}$	1.16(0.13)	$4.12(0.91) \times 10^{-2}$
17(1)	2.05(0.20)	1.03(0.11)	$4.30(0.49) \times 10^{-1}$	$4.36(0.60) \times 10^{-1}$	$8.65(0.98) \times 10^{-1}$	$2.84(0.63) \times 10^{-2}$
19(1)	1.64(0.16)	$7.98(0.87) \times 10^{-1}$	$3.22(0.37) \times 10^{-1}$	$3.02(0.41) \times 10^{-1}$	$5.84(0.63) \times 10^{-1}$	$1.52(0.34) \times 10^{-2}$
21(1)	1.49(0.14)	$7.26(0.79) \times 10^{-1}$	$2.79(0.32) \times 10^{-1}$	$2.59(0.35) \times 10^{-1}$	$4.73(0.51) \times 10^{-1}$	$1.16(0.26) \times 10^{-2}$
23(1)	1.25(0.12)	$5.90(0.64) \times 10^{-1}$	$2.21(0.25) \times 10^{-1}$	$1.90(0.26) \times 10^{-1}$	$3.62(0.38) \times 10^{-1}$	$7.7(1.7) \times 10^{-3}$
27(1)	$9.48(0.91) \times 10^{-1}$	$4.36(0.48) \times 10^{-1}$	$1.55(0.18) \times 10^{-1}$	$1.24(0.17) \times 10^{-1}$	$2.41(0.25) \times 10^{-1}$	$3.31(0.74) \times 10^{-3}$
31(1)	$7.70(0.74) \times 10^{-1}$	$3.36(0.37) \times 10^{-1}$	$1.16(0.13) \times 10^{-1}$	$8.9(1.2) \times 10^{-2}$	$1.71(0.18) \times 10^{-1}$	$2.19(0.50) \times 10^{-3}$
35(1)	$6.50(0.63) \times 10^{-1}$	$2.70(0.29) \times 10^{-1}$	$9.0(1.0) \times 10^{-2}$	$6.58(0.89) \times 10^{-2}$	$1.32(0.14) \times 10^{-1}$	$1.40(0.31) \times 10^{-3}$
39(1)	$5.48(0.53) \times 10^{-1}$	$2.17(0.24) \times 10^{-1}$	$7.03(0.81) \times 10^{-2}$	$4.93(0.67) \times 10^{-2}$	$9.8(1.0) \times 10^{-2}$	$8.5(1.9) \times 10^{-4}$

θ (deg)	^{6}Li $d\sigma/d\Omega$ (b sr^{-1})	^{7}Li $d\sigma/d\Omega$ (b sr^{-1})	^{7}Be $d\sigma/d\Omega$ (b sr^{-1})	^{9}Be $d\sigma/d\Omega$ (b sr^{-1})	^{10}Be $d\sigma/d\Omega$ (b sr^{-1})	^{8}B $d\sigma/d\Omega$ (b sr^{-1})
4(1)	1.17(0.15)	1.13(0.15)	$9.68(0.97) \times 10^{-1}$	$4.10(0.43) \times 10^{-1}$	$2.26(0.30) \times 10^{-1}$	$1.31(0.35) \times 10^{-1}$
7(1)	$4.56(0.62) \times 10^{-1}$	$4.41(0.60) \times 10^{-1}$	$3.83(0.40) \times 10^{-1}$	$1.56(0.17) \times 10^{-1}$	$7.6(1.0) \times 10^{-2}$	$6.6(1.8) \times 10^{-2}$
9(1)	$2.68(0.36) \times 10^{-1}$	$2.55(0.35) \times 10^{-1}$	$2(0.21) \times 10^{-1}$	$6.37(0.70) \times 10^{-2}$	$3.08(0.42) \times 10^{-2}$	$2.41(0.64) \times 10^{-2}$
11(1)	$1.40(0.19) \times 10^{-1}$	$1.21(0.16) \times 10^{-1}$	$8.16(0.85) \times 10^{-2}$	$1.89(0.21) \times 10^{-2}$	$8.2(1.1) \times 10^{-3}$	$7.8(2.1) \times 10^{-3}$
13(1)	$8.8(1.2) \times 10^{-2}$	$7.18(0.98) \times 10^{-2}$	$4.60(0.48) \times 10^{-2}$	$9.1(1.0) \times 10^{-3}$	$3.50(0.50) \times 10^{-3}$	$3.58(0.97) \times 10^{-3}$
15(1)	$5.35(0.73) \times 10^{-2}$	$4.29(0.58) \times 10^{-2}$	$2.38(0.25) \times 10^{-2}$	$3.74(0.44) \times 10^{-3}$	$1.68(0.24) \times 10^{-3}$	$1.57(0.48) \times 10^{-3}$
17(1)	$3.80(0.52) \times 10^{-2}$	$2.95(0.40) \times 10^{-2}$	$1.57(0.16) \times 10^{-2}$	$2.99(0.34) \times 10^{-3}$	$1.28(0.19) \times 10^{-3}$	$1.05(0.31) \times 10^{-3}$
19(1)	$2.57(0.35) \times 10^{-2}$	$2.07(0.28) \times 10^{-2}$	$9.9(1.0) \times 10^{-3}$	$1.82(0.22) \times 10^{-3}$	$7.8(1.2) \times 10^{-4}$	$6.7(2.0) \times 10^{-4}$
21(1)	$1.99(0.27) \times 10^{-2}$	$1.57(0.21) \times 10^{-2}$	$7.17(0.77) \times 10^{-3}$	$1.67(0.20) \times 10^{-3}$	$6.5(1.0) \times 10^{-4}$	$5.3(1.6) \times 10^{-4}$
23(1)	$1.53(0.21) \times 10^{-2}$	$1.26(0.17) \times 10^{-2}$	$5.36(0.56) \times 10^{-3}$	$1.07(0.12) \times 10^{-3}$	$5.81(0.84) \times 10^{-4}$	$3.09(0.85) \times 10^{-4}$
27(1)	$9.4(1.3) \times 10^{-3}$	$7.9(1.1) \times 10^{-3}$	$3.18(0.36) \times 10^{-3}$	$7.7(1.1) \times 10^{-4}$	$3.74(0.70) \times 10^{-4}$	$1.06(0.38) \times 10^{-4}$
31(1)	$5.82(0.82) \times 10^{-3}$	$5.35(0.75) \times 10^{-3}$	$2.05(0.25) \times 10^{-3}$	$4.41(0.76) \times 10^{-4}$	$1.89(0.46) \times 10^{-4}$	$1.18(0.44) \times 10^{-4}$
35(1)	$4.18(0.58) \times 10^{-3}$	$3.52(0.49) \times 10^{-3}$	$1.35(0.15) \times 10^{-3}$	$2.75(0.41) \times 10^{-4}$	$1.34(0.26) \times 10^{-4}$	$5.1(1.8) \times 10^{-5}$
39(1)	$2.86(0.40) \times 10^{-3}$	$2.71(0.38) \times 10^{-3}$	$8.4(1.0) \times 10^{-4}$	$1.58(0.28) \times 10^{-4}$	$5.5(1.5) \times 10^{-5}$	$3.2(1.3) \times 10^{-5}$

θ (deg)	^{10}B $d\sigma/d\Omega$ (b sr^{-1})	^{11}B $d\sigma/d\Omega$ (b sr^{-1})	^{10}C $d\sigma/d\Omega$ (b sr^{-1})	^{11}C $d\sigma/d\Omega$ (b sr^{-1})	^{12}C $d\sigma/d\Omega$ (b sr^{-1})
4(1)	1.18(0.16)	1.62(0.21)	$2.11(0.46) \times 10^{-1}$	1.35(0.18)	1.96(0.26)
7(1)	$2.70(0.37) \times 10^{-1}$	$2.42(0.33) \times 10^{-1}$	$4.7(1.0) \times 10^{-2}$	$1.88(0.25) \times 10^{-1}$	$1.56(0.21) \times 10^{-1}$
9(1)	$8.3(1.1) \times 10^{-2}$	$6.99(0.95) \times 10^{-2}$	$1.22(0.27) \times 10^{-2}$	$4.60(0.63) \times 10^{-2}$	$2.87(0.47) \times 10^{-2}$
11(1)	$2.17(0.30) \times 10^{-2}$	$1.40(0.19) \times 10^{-2}$	$2.85(0.64) \times 10^{-3}$	$8.2(1.1) \times 10^{-3}$	$3.08(0.83) \times 10^{-3}$
13(1)	$8.4(1.2) \times 10^{-3}$	$4.63(0.67) \times 10^{-3}$	$9.2(2.7) \times 10^{-4}$	$2.27(0.40) \times 10^{-3}$	–
15(1)	$3.42(0.49) \times 10^{-3}$	$2.34(0.34) \times 10^{-3}$	$2.9(1.3) \times 10^{-4}$	$7.8(1.5) \times 10^{-4}$	–
17(1)	$2.16(0.32) \times 10^{-3}$	$1.55(0.24) \times 10^{-3}$	$3.7(1.0) \times 10^{-4}$	$4.9(1.1) \times 10^{-4}$	–
19(1)	$1.37(0.21) \times 10^{-3}$	$1.15(0.18) \times 10^{-3}$	$2.05(0.55) \times 10^{-4}$	$3.16(0.66) \times 10^{-4}$	–
21(1)	$1.18(0.18) \times 10^{-3}$	$8.9(1.4) \times 10^{-4}$	$1.29(0.43) \times 10^{-4}$	$2.69(0.52) \times 10^{-4}$	–
23(1)	$9.4(1.3) \times 10^{-4}$	$7.4(1.1) \times 10^{-4}$	$9.3(2.4) \times 10^{-5}$	$1.94(0.31) \times 10^{-4}$	–
27(1)	$5.24(0.91) \times 10^{-4}$	$4.06(0.75) \times 10^{-4}$	$6.9(2.6) \times 10^{-5}$	$1.06(0.29) \times 10^{-4}$	–
31(1)	$3.15(0.66) \times 10^{-4}$	$1.65(0.42) \times 10^{-4}$	$1.6(1.2) \times 10^{-5}$	$9.4(3.0) \times 10^{-5}$	–
35(1)	$2.06(0.36) \times 10^{-4}$	$1.36(0.27) \times 10^{-4}$	$1.07(0.58) \times 10^{-5}$	$2.67(0.92) \times 10^{-5}$	–
39(1)	$1.26(0.26) \times 10^{-4}$	$6.7(1.7) \times 10^{-5}$	$5.8(4.3) \times 10^{-6}$	$1.46(0.68) \times 10^{-5}$	–

APPENDIX E: CROSS SECTION FOR THE TITANIUM TARGET

TABLE X. ^{12}C fragmentation cross sections for the titanium target at different angles. The values in parentheses represent the uncertainties [4.55(0.52) is equivalent to 4.55 ± 0.52].

θ (deg)	^{1}H $d\sigma/d\Omega$ (b sr^{-1})	^{2}H $d\sigma/d\Omega$ (b sr^{-1})	^{3}H $d\sigma/d\Omega$ (b sr^{-1})	^{3}He $d\sigma/d\Omega$ (b sr^{-1})	^{4}He $d\sigma/d\Omega$ (b sr^{-1})	^{6}He $d\sigma/d\Omega$ (b sr^{-1})
4(1)	8.24(0.75)	4.80(0.50)	2.33(0.26)	3.12(0.67)	$1.90(0.26) \times 10^{1}$	$6.5(3.9) \times 10^{-1}$
7(1)	5.79(0.56)	3.25(0.35)	1.79(0.21)	2.24(0.38)	8.3(1.1)	$6.4(1.8) \times 10^{-1}$
9(1)	5.37(0.52)	2.92(0.32)	1.48(0.17)	1.77(0.29)	5.75(0.75)	$4.1(1.0) \times 10^{-1}$
11(1)	4.35(0.42)	2.31(0.25)	1.14(0.13)	1.24(0.18)	3.39(0.41)	$1.66(0.38) \times 10^{-1}$
13(1)	3.88(0.37)	2.03(0.22)	$9.5(1.1) \times 10^{-1}$	$9.7(1.4) \times 10^{-1}$	2.37(0.29)	$1.15(0.26) \times 10^{-1}$
15(1)	3.13(0.30)	1.63(0.18)	$7.54(0.87) \times 10^{-1}$	$6.97(0.97) \times 10^{-1}$	1.56(0.18)	$5.6(1.2) \times 10^{-2}$
17(1)	2.80(0.27)	1.44(0.16)	$6.36(0.73) \times 10^{-1}$	$5.69(0.79) \times 10^{-1}$	1.18(0.13)	$4.12(0.91) \times 10^{-2}$
19(1)	2.28(0.22)	1.17(0.13)	$5.08(0.58) \times 10^{-1}$	$4.16(0.57) \times 10^{-1}$	$8.54(0.93) \times 10^{-1}$	$2.33(0.52) \times 10^{-2}$
21(1)	2.08(0.20)	1.04(0.11)	$4.25(0.49) \times 10^{-1}$	$3.51(0.48) \times 10^{-1}$	$6.79(0.74) \times 10^{-1}$	$1.75(0.40) \times 10^{-2}$
23(1)	1.73(0.17)	$8.51(0.93) \times 10^{-1}$	$3.46(0.40) \times 10^{-1}$	$2.60(0.35) \times 10^{-1}$	$5.34(0.57) \times 10^{-1}$	$1.17(0.26) \times 10^{-2}$
27(1)	1.36(0.13)	$6.39(0.70) \times 10^{-1}$	$2.47(0.28) \times 10^{-1}$	$1.72(0.23) \times 10^{-1}$	$3.69(0.38) \times 10^{-1}$	$6.7(1.5) \times 10^{-3}$
31(1)	1.12(0.11)	$4.99(0.55) \times 10^{-1}$	$1.83(0.21) \times 10^{-1}$	$1.24(0.17) \times 10^{-1}$	$2.71(0.28) \times 10^{-1}$	$3.77(0.86) \times 10^{-3}$
35(1)	$9.66(0.93) \times 10^{-1}$	$4.09(0.45) \times 10^{-1}$	$1.46(0.17) \times 10^{-1}$	$9.4(1.3) \times 10^{-2}$	$2.10(0.22) \times 10^{-1}$	$2.78(0.62) \times 10^{-3}$
39(1)	$8.30(0.80) \times 10^{-1}$	$3.31(0.36) \times 10^{-1}$	$1.14(0.13) \times 10^{-1}$	$7.02(0.95) \times 10^{-2}$	$1.60(0.17) \times 10^{-1}$	$1.83(0.41) \times 10^{-3}$

θ (deg)	^{6}Li $d\sigma/d\Omega$ (b sr^{-1})	^{7}Li $d\sigma/d\Omega$ (b sr^{-1})	^{7}Be $d\sigma/d\Omega$ (b sr^{-1})	^{9}Be $d\sigma/d\Omega$ (b sr^{-1})	^{10}Be $d\sigma/d\Omega$ (b sr^{-1})	^{8}B $d\sigma/d\Omega$ (b sr^{-1})
4(1)	1.37(0.18)	1.29(0.17)	1.07(0.11)	$4.98(0.53) \times 10^{-1}$	$2.56(0.34) \times 10^{-1}$	$1.42(0.38) \times 10^{-1}$
7(1)	$4.98(0.68) \times 10^{-1}$	$5.13(0.69) \times 10^{-1}$	$4.24(0.44) \times 10^{-1}$	$1.73(0.19) \times 10^{-1}$	$9.8(1.3) \times 10^{-2}$	$7.1(1.9) \times 10^{-2}$
9(1)	$3.21(0.43) \times 10^{-1}$	$3.13(0.42) \times 10^{-1}$	$2.26(0.24) \times 10^{-1}$	$7.95(0.88) \times 10^{-2}$	$3.46(0.47) \times 10^{-2}$	$2.69(0.72) \times 10^{-2}$
11(1)	$1.68(0.23) \times 10^{-1}$	$1.57(0.21) \times 10^{-1}$	$9.5(1.0) \times 10^{-2}$	$2.45(0.27) \times 10^{-2}$	$1.20(0.17) \times 10^{-2}$	$8.6(2.3) \times 10^{-3}$
13(1)	$1.15(0.16) \times 10^{-1}$	$9.6(1.3) \times 10^{-2}$	$5.43(0.57) \times 10^{-2}$	$1.31(0.15) \times 10^{-2}$	$5.91(0.85) \times 10^{-3}$	$4.1(1.1) \times 10^{-3}$
15(1)	$6.94(0.94) \times 10^{-2}$	$6.18(0.84) \times 10^{-2}$	$3.01(0.32) \times 10^{-2}$	$6.41(0.72) \times 10^{-3}$	$3.20(0.45) \times 10^{-3}$	$2.27(0.61) \times 10^{-3}$
17(1)	$5.25(0.71) \times 10^{-2}$	$4.33(0.59) \times 10^{-2}$	$2.02(0.21) \times 10^{-2}$	$4.45(0.50) \times 10^{-3}$	$2.32(0.33) \times 10^{-3}$	$1.68(0.45) \times 10^{-3}$
19(1)	$3.71(0.50) \times 10^{-2}$	$3.29(0.45) \times 10^{-2}$	$1.29(0.14) \times 10^{-2}$	$3.08(0.36) \times 10^{-3}$	$1.60(0.24) \times 10^{-3}$	$1.01(0.30) \times 10^{-3}$
21(1)	$2.88(0.39) \times 10^{-2}$	$2.42(0.33) \times 10^{-2}$	$9.5(1.1) \times 10^{-3}$	$2.23(0.34) \times 10^{-3}$	$1.26(0.24) \times 10^{-3}$	$4.7(3.3) \times 10^{-4}$
23(1)	$2.24(0.30) \times 10^{-2}$	$1.98(0.27) \times 10^{-2}$	$7.14(0.76) \times 10^{-3}$	$1.89(0.22) \times 10^{-3}$	$1.16(0.17) \times 10^{-3}$	$3.9(1.1) \times 10^{-4}$
27(1)	$1.32(0.18) \times 10^{-2}$	$1.21(0.17) \times 10^{-2}$	$4.33(0.51) \times 10^{-3}$	$1.15(0.18) \times 10^{-3}$	$7.6(1.4) \times 10^{-4}$	$1.79(0.68) \times 10^{-4}$
31(1)	$8.9(1.3) \times 10^{-3}$	$7.9(1.1) \times 10^{-3}$	$2.93(0.37) \times 10^{-3}$	$8.3(1.4) \times 10^{-4}$	$6.2(1.2) \times 10^{-4}$	$1.54(0.62) \times 10^{-4}$
35(1)	$6.77(0.93) \times 10^{-3}$	$6.59(0.90) \times 10^{-3}$	$1.98(0.22) \times 10^{-3}$	$6.05(0.80) \times 10^{-4}$	$3.13(0.54) \times 10^{-4}$	$7.6(2.6) \times 10^{-5}$
39(1)	$4.71(0.65) \times 10^{-3}$	$4.62(0.64) \times 10^{-3}$	$1.25(0.15) \times 10^{-3}$	$3.98(0.56) \times 10^{-4}$	$2.64(0.46) \times 10^{-4}$	$7.8(2.6) \times 10^{-5}$

θ (deg)	^{10}B $d\sigma/d\Omega$ (b sr^{-1})	^{11}B $d\sigma/d\Omega$ (b sr^{-1})	^{10}C $d\sigma/d\Omega$ (b sr^{-1})	^{11}C $d\sigma/d\Omega$ (b sr^{-1})	^{12}C $d\sigma/d\Omega$ (b sr^{-1})
4(1)	1.35(0.18)	1.66(0.22)	$2.45(0.54) \times 10^{-1}$	1.40(0.19)	1.86(0.28)
7(1)	$2.59(0.35) \times 10^{-1}$	$3.04(0.41) \times 10^{-1}$	$4.13(0.91) \times 10^{-2}$	$1.77(0.24) \times 10^{-1}$	$1.96(0.27) \times 10^{-1}$
9(1)	$1.03(0.14) \times 10^{-1}$	$7.6(1.0) \times 10^{-2}$	$1.46(0.32) \times 10^{-2}$	$5.95(0.81) \times 10^{-2}$	$4.58(0.62) \times 10^{-2}$
11(1)	$2.45(0.34) \times 10^{-2}$	$2(0.28) \times 10^{-2}$	$3.06(0.70) \times 10^{-3}$	$1.03(0.14) \times 10^{-2}$	$1.92(0.26) \times 10^{-2}$
13(1)	$1.26(0.18) \times 10^{-2}$	$6.66(0.95) \times 10^{-3}$	$1.74(0.41) \times 10^{-3}$	$4.66(0.68) \times 10^{-3}$	$1.44(0.20) \times 10^{-2}$
15(1)	$4.71(0.65) \times 10^{-3}$	$3.80(0.53) \times 10^{-3}$	$6.8(1.6) \times 10^{-4}$	$1.39(0.20) \times 10^{-3}$	$10.0(1.4) \times 10^{-3}$
17(1)	$3.58(0.50) \times 10^{-3}$	$2.64(0.37) \times 10^{-3}$	$6.7(1.5) \times 10^{-4}$	$1.28(0.19) \times 10^{-3}$	–
19(1)	$2.30(0.36) \times 10^{-3}$	$2.19(0.33) \times 10^{-3}$	$2.8(1.1) \times 10^{-4}$	$4.6(1.2) \times 10^{-4}$	–
21(1)	$1.66(0.31) \times 10^{-3}$	$1.18(0.26) \times 10^{-3}$	$1.7(1.3) \times 10^{-4}$	$5.43(16.0) \times 10^{-5}$	–
23(1)	$1.43(0.21) \times 10^{-3}$	$1.33(0.19) \times 10^{-3}$	$1.51(0.41) \times 10^{-4}$	$2.77(0.49) \times 10^{-4}$	–
27(1)	$9.1(1.6) \times 10^{-4}$	$4.9(1.0) \times 10^{-4}$	$5.1(2.8) \times 10^{-5}$	$2.18(0.61) \times 10^{-4}$	–
31(1)	$4.8(1.0) \times 10^{-4}$	$5.5(1.1) \times 10^{-4}$	$7.0(3.5) \times 10^{-5}$	$5.6(2.9) \times 10^{-5}$	–
35(1)	$3.23(0.55) \times 10^{-4}$	$3.13(0.54) \times 10^{-4}$	$2.8(1.1) \times 10^{-5}$	$6.5(1.7) \times 10^{-5}$	–
39(1)	$2.87(0.49) \times 10^{-4}$	$1.79(0.34) \times 10^{-4}$	$2.9(1.2) \times 10^{-5}$	$1.96(0.84) \times 10^{-5}$	–

[1] D. Schardt *et al*., Adv. Space Res. **17**, 87 (1996).
[2] M. Scholz, Nucl. Instrum. Methods Phys. Res. B **161–163**, 76 (2000).
[3] T. T. Böhlen, F. Cerutti, M. Dosanjh, A. Ferrari, I. Gudowska, A. Mairani, and J. M. Quesada, Phys. Med. Biol. **55**, 5833 (2010).
[4] B. Braunn A. Boudard, J. Colin, J. Cugnon, D. Cussol, J. C. David, P. Kaitaniemi, M. Labalme, S. Leray, and D. Mancusi, J. Physique: Conference Series **420**, 012163 (2013).
[5] M. de Napoli *et al*., Phys. Med. Biol. **57**, 7651 (2012).
[6] N. Matsufuji, A. Fukumura, M. Komori, T. Kanai, and T. Kohno, Phys. Med. Biol. **48**, 1605 (2003).
[7] N. Matsufuji *et al*., Phys. Med. Biol. **50**, 3393 (2005).
[8] T. Toshito *et al*., Phys. Rev. C **75**, 054606 (2007).
[9] I. Schall *et al*., Nucl. Instrum. Methods Phys. Res. B **117**, 221 (1996).
[10] K. Gunzert-Marx, D. Schardt, and R. S. Simon, Rad. Prot. Dosim. **110**, 595 (2004).
[11] K. Gunzert-Marx, H. Iwase, D. Schardt, and R. S. Simon, New J. Phys. **10**, 075003 (2008).
[12] B. Braunn *et al*., Nucl. Instrum. Methods Phys. Res. B **269**, 2676 (2011).
[13] G. Battistoni, F. Cerutti, A. Fasso, A. Ferrari, S. Muraro, J. Ranft, S. Roesler, and P. R. Sala, AIP Conf. Proc. **896**, 31 (2007).
[14] A. Boudard, J.-Cugnon, J. C. David, S. Leray, and D. Mancusi, Phys. Rev. C **87**, 014606 (2013).
[15] S. Agostinelli *et al*., Nucl. Instrum. Methods Phys. Res. A **506**, 250 (2003).
[16] B. Braunn, Ph.D. thesis, Université de Caen Basse Normandie, 2010.
[17] R. Pleskac *et al*., Nucl. Instrum. Methods Phys. Res. A **678**, 130 (2012).
[18] J. Dudouet *et al*., Nucl. Instrum. Methods Phys. Res. A **715**, 98 (2013).
[19] J. Pouthas *et al*., Nucl. Instrum. Methods Phys. Res. A **357**, 418 (1995).
[20] J. Franckland *et al*., KaliVeda data analysis framework. http://indra.in2p3.fr/KaliVedaDoc.
[21] G. Folger, V. N. Ivanchenko, and J. P. Wellisch, Eur. Phys. J. A **21**, 407 (2004).
[22] T. Koi *et al*., Joint International Conference on Supercomputing in Nuclear Applications and Monte Carlo 2010 (SNA + MC2010) Hitotsubashi Memorial Hall, Tokyo, Japan, 2010 (Atomic Energy Society of Japan, Japan, 2010).
[23] J. Birks, *The Theory and Practice of Scintillation Counting* (Pergamon Press, Oxford, 1964).
[24] I. Antcheva *et al*., Comput. Phys. Commun. **180**, 2499 (2009).
[25] M. Parlog *et al*., Nucl. Instrum. Methods Phys. Res. B **482**, 693 (2002).
[26] M. Golovkov, D. Aleksandrov, L. Chulkov, G. Kraus, and D. Schardt, *1st International Week on Hadrontherapy: Advances in Hadron Therapy, Archamps, France, 1995* (CERN, Geneva, 1997), pp. 316–324.